# High Order Finite Element Method for solving Convected Helmholtz equation in radial and axisymmetric domains. Application to Helioseismology

Juliette Chabassier, Marc Duruflé


# High Order Finite Element Method for solving Convected Helmholtz equation in radial and axisymmetric domains. Application to Helioseismology.

**Juliette Chabassier, Marc Duruflé**

**RESEARCH REPORT**

**N° 8893**

March 2016

Project-Teams Magique3D

ISSN 0249-6399 ISRN INRIA/RR--8893--FR+ENG

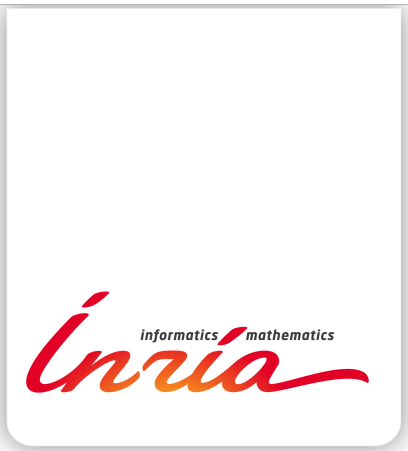


# High Order Finite Element Method for solving Convected Helmholtz equation in radial and axisymmetric domains. Application to Helioseismology.

Juliette Chabassier*, Marc Duruflé†

Project-Teams Magique3D

Research Report n° 8893 — March 2016 — 44 pages

**Abstract:** This document concerns the solution of convected Helmholtz equation for radial or axisymmetric configuration. After setting the considered problem and the associated equations, we propose in section 2 a numerical method adapted for geometries that only vary radially. Then in section 3 we propose a numerical method for geometries with an axial symmetry. In these two situations, the solution is computed with finite elements after having been decomposed on a basis of orthogonal modes : spherical harmonics in the radial geometry and Fourier modes in the axisymmetric geometry. The number of required modes depends on the configuration (and especially location) of the source. The two methods are tested on the computation of Green's functions for which analytical solutions are available for quantitative comparison. The methods are then compared in section 4 with the classical 3D finite elements method, and the performances are assessed for an academic test case, showing the advantages of each method in terms of computation time and memory usage. In the context of helioseismology, the perturbation of the fluid displacement in the sun can be modeled accurately by Galbrun's equations. We show in section 5 that under some assumptions on the background medium, the Galbrun's equations can be simplified to an equation that has the same variational formulation as the one treated in the first part of this document. Numerical simulations are done in this realistic configuration, and the different methods of resolution are compared.

**Key-words:** finite elements, convected Helmholtz equation, axisymmetric geometry, radial geometry, helioseismology

* University of Pau, INRIA Bordeaux Sud-Ouest, EPI Magique 3-D
† University of Bordeaux, INRIA Bordeaux Sud-Ouest, EPI Magique 3-D

RESEARCH CENTRE
BORDEAUX – SUD-OUEST

200 avenue de la Vieille Tour
33405 Talence Cedex

# Eléments finis d'ordre élevé pour l'équation de Helmholtz convectée dans des domaines radiaux et axisymétriques. Application à l'héliosismologie

**Résumé :** Ce document traite la résolution de l'équation de Helmholtz convectée pour des géométries radiales ou axisymétriques. Après avoir établi le problème considéré et les équations associées, nous proposons en section 2 une méthode numérique adaptée pour les géométries qui varient uniquement dans la direction radiale. Ensuite en section 3 nous proposons une méthode pour les géométries présentant une symétrie axiale. Dans ces deux situations, la solution est calculée avec des éléments finis après l'avoir décomposée sur une base de modes orthogonaux : les harmoniques sphériques pour la géométrie radiale et les modes de Fourier pour la géométrie axi-symétrique. Le nombre de modes nécessaires dépend de la configuration (et en particulier de la localisation) de la source. Les deux méthodes sont testées sur le calcul de la fonction de Green, pour laquelle des solutions analytiques sont disponibles pour une comparaison quantitative. Les méthodes sont ensuite comparées en section 4 avec les éléments finis classiques en 3D, et les performances sont comparées sur un cas test académique, montrant les avantages de chaque méthode en termes de temps de calcul et d'utilisation mémoire. Dans le contexte de l'héliosismologie, les équations de Galbrun sont une bonne modélisation de la perturbation du déplacement fluide dans le Soleil. Nous montrons en section 5 que sous certaines hypothèses sur le milieu quasi-stationnaire, les équations de Galbrun peuvent se simplifier en une équation qui admet la même formulation variationnelle que l'équation traitée dans la première partie de ce document. Des simulations numériques sont effectuées dans cette situation réaliste, et les différentes méthodes de résolution sont comparées.

**Mots-clés :** éléments finis, équation de Helmholtz convectée, géométrie axisymétrique, géométrie radiale, héliosismologie

# Contents

# 1 General setting

We are interested in solving the convected Helmholtz equation in a three-dimensional domain $\Omega$:

$$-\omega^2\widetilde{\rho}u - 2i\omega\widetilde{M}\cdot\nabla u + \widetilde{M}\cdot\nabla\left(\widetilde{\beta}\widetilde{M}\cdot\nabla u\right) - \mathrm{div}\left(\widetilde{\mu}\nabla u\right) = f \tag{1}$$

where $\omega$ is the pulsation, $\widetilde{\rho}$ and $\widetilde{\beta}$ are complex fields, $\widetilde{\mu}$ is a complex tensor (a symmetric matrix of size $3\times 3$), $\widetilde{M}$ a complex vector. These fields are assumed to be known and depend on the space variable $x$. Let us assume that the vector $\widetilde{M}$ has a null divergence and such that its normal component vanishes on the boundary $\Gamma$ of the domain $\Omega$:

$$\mathrm{div}\widetilde{M} = 0 \ \text{ in } \Omega, \quad \widetilde{M}\cdot n = 0 \ \text{ in } \Gamma$$

This equation is solved with continuous finite elements by searching u in $H^1(\Omega)$. The variational formulation is obtained by multiplying by the conjugate of a test function $v\in H^1(\Omega)$, integrating over the computational domain $\Omega$ and performing an integration by parts. The problem becomes: Find $u\in H^1(\Omega)$ such that for all $v\in H^1(\Omega)$,

$$\begin{aligned}-\omega^2\int_\Omega \widetilde{\rho}u\,\bar{v}\,dx - i\omega\int_\Omega \widetilde{M}\cdot\nabla u\,\bar{v}\,dx + i\omega\int_\Omega \widetilde{M}\cdot\nabla\bar{v}\,u\,dx - \int_\Omega \widetilde{\beta}\,\widetilde{M}\cdot\nabla u\,\widetilde{M}\cdot\nabla\bar{v}\,dx \\ + \int_\Omega \widetilde{\mu}\nabla u\cdot\nabla\bar{v}\,dx - \int_\Gamma \widetilde{\mu}\frac{\partial u}{\partial n}\bar{v}\,dx = \int_\Omega f\bar{v}\,dx\end{aligned} \tag{2}$$

In the section 5, we describe how we obtain this variational formulation in helioseismology context. This variational formulation is obtained with the following choice of dimensioned fields:

$$\widetilde{\rho} = \frac{1}{\rho c^2}\left(1+\frac{2i\gamma}{\omega}\right),\ \widetilde{M} = \frac{M}{\rho c^2},\ \widetilde{\mu} = \frac{1}{\rho},\ \widetilde{\beta} = \rho c^2$$

where $\rho$ is the background density, $c$ the sound speed, $\gamma$ a damping coefficient and $M$ the flow. The boundary term in the variational formulation is replaced by the appropriate term depending on the boundary condition imposed on $\Gamma$.

The computations will be performed for a ball of radius $R$. In this report, for the sake of simplicity, on the outer sphere of radius $R$, we will consider either Neumann boundary condition

$$\frac{\partial u}{\partial n} = 0$$

or absorbing boundary condition

$$\frac{\partial u}{\partial n} - ik(\omega)u = 0$$

The wave number $k(\omega)$ is given as

$$k(\omega) = \omega\sqrt{\frac{\widetilde{\rho}}{\widetilde{\mu}}}$$

Two types of sources will be either a Dirac :

$$f = \delta_{x=y}$$

where $y$ is the Dirac's origin, either an incident plane wave (for a null flow) :

$$f = \omega^2(\widetilde{\rho}-\rho_0)u^{\mathrm{inc}} + \mathrm{div}\left((\widetilde{\mu}-\mu_0)\nabla u^{\mathrm{inc}}\right)$$

with

$$u^{\text{inc}} = exp(i\vec{k} \cdot x)$$

where $\vec{k}$ is the wave vector given as:

$$\vec{k} = k_0(\omega)\vec{u}$$

where $\vec{u}$ is an unit vector (the direction of the incident wave), $\rho_0, \mu_0, k_0(\omega)$ are the values at infinity (usually values at $r = R$).

# 2 Solution with radial symmetry (1.5D)

In this section, we assume that the coefficients depend only on the radius $r$, we use the spherical coordinates $(r, \theta, \phi)$ which are related to the cartesian coordinates with the relations

$$\begin{cases} x = r\, \sin\theta \cos\phi \\ y = r\, \sin\theta \sin\phi \\ z = r\, \cos\theta \end{cases}$$

We consider that the flow $\widetilde{M}$ is null, since a flow depending only on $r$ and oriented along unit vectors of spherical coordinates is not interesting for our applications. The interval $[0, R]$ is subdivided into sub-intervals :

$$[0, R] = \cup [x_i, x_{i+1}]$$

One-dimensional finite elements will be used in $r$-coordinate, while spherical harmonics will be used in $\theta$, $\phi$. Since spherical harmonics are orthonormal and diagonalize the laplacian, we will obtain a decoupled sequence of 1-D problems to solve.

## 2.1 Discretization

The 1-D finite element space is equal to

$$V_h \;=\; \left\{ u \in H^1([0, R]) \text{ such that } u|_{[x_i, x_i+1]} \in \mathbb{P}_r \right\}$$

where $\mathbb{P}_r$ is the space of polynomials of degree lower or equal to $r$. $r$ is the order of the approximation. The solution $u$ is then searched under the form

$$u(r, \theta, \phi) = \sum_{j=0}^{N_h} \sum_{\ell=0}^{L} \sum_{m=-\ell}^{\ell} u_j^{\ell,m}\, \varphi_j(r)\, Y_\ell^m(\theta, \phi)$$

where $\varphi_i$ are basis functions generating the finite element space $V_h$ of dimension $N_h$, and $Y_\ell^m$ spherical harmonics given as

$$Y_\ell^m(\theta, \phi) = (-1)^m \sqrt{\frac{(2\ell + 1)}{4\pi} \frac{(\ell - m)!}{(\ell + m)!}} P_\ell^m(\cos\theta) e^{im\phi}$$

where $P_\ell^m$ are the associated Legendre polynomials. $L$ is the maximal degree of spherical harmonics used in the expression of $u$. The Laplacian operator applied to a basis function can be computed :

$$\text{div}\left(\widetilde{\mu} \nabla \left[\varphi_i(r)\, Y_\ell^m(\theta, \phi)\right]\right) \;=\; \left[\frac{1}{r^2} \frac{\partial}{\partial r} \left(\widetilde{\mu}\, r^2 \frac{\partial \varphi_i(r)}{\partial r}\right) - \frac{\widetilde{\mu} \ell(\ell + 1)}{r^2}\right] Y_\ell^m(\theta, \phi)$$

Let us denote

$$u^{\ell,m} = \sum_{j=0}^{N_h} u_j^{\ell,m}\, \varphi_j(r)$$

The variational formulation is obtained by multiplying Helmholtz equation written in spherical coordinates with $r^2 \sin\theta\ \bar{Y_\ell^m}(\theta,\phi)$ and performing an integration by parts. Since spherical harmonics are orthonormal with respect to the weight $r^2\sin\theta$, we obtain the following variational formulation. Find $u^{\ell,m}$ such that $\forall \varphi_i \in V_h$:

$$-\omega^2 \int_0^R \widetilde{\rho}\, r^2\, u^{\ell,m}\varphi_i\, dr + \int_0^R \widetilde{\mu}\, r^2 \frac{\partial u^{\ell,m}}{\partial r}\frac{\partial \varphi_i}{\partial r}\, dr + \ell(\ell{+}1) \int_0^R \widetilde{\mu}\, u^{\ell,m}\varphi_i\, dr - \left[\widetilde{\mu}\, r^2 \frac{\partial u^{\ell,m}}{\partial r}\varphi_i\right]_0^R = f_i^{\ell,m}$$

where

$$f_i^{\ell,m} = \int_0^R \int_0^\pi \int_0^{2\pi} r^2\, f(r,\theta,\phi)\bar{Y}_\ell^m(\theta,\phi)\, \sin\theta\, d\phi d\theta dr$$

The boundary term vanishes for Neumann condition. For an absorbing boundary condition, it becomes

$$-ik(\omega)\,\widetilde{\mu}\, R^2\, u^{\ell,m}(R)\,\varphi_i(R)$$

## 2.2 1-D finite element method

For the discretization of the finite element space $V_h$, Gauss-Lobatto points are used both for interpolation and quadrature such that the evaluation of finite element matrices is a bit faster. Let us denote $(\hat{\xi}_k, \omega_k)_{1\le k\le r+1}$ the Gauss-Lobatto quadrature formulas of degree $r$, $\hat{\xi}_k$ being Gauss-Lobatto points, and $\omega_k$ their associated weights. The associated quadrature formula is exact for polynomials in $\mathbb{P}_{2r-1}$, and is denoted as:

$$\oint_0^1 f(r)dr \ = \ \sum_{k=1}^{r+1} \omega_k f(\hat{\xi}_k)$$

On the interval $[r_e, r_{e+1}]$, Gauss-Lobatto points $\xi_k$ are given as

$$\xi_k \ = \ r_e + \hat{\xi}_k(r_{e+1} - r_e)$$

On this interval, basis functions are Lagrange interpolatory polynomials:

$$\varphi_i(r) \ = \ \frac{\displaystyle\prod_{j=1, j\neq i}^{r+1} (r - \xi_j)}{\displaystyle\prod_{j=1, j\neq i}^{r+1} (\xi_i - \xi_j)}$$

such that they satisfy the relation

$$\varphi_i(\xi_j) = \delta_{i,j}$$

where $\delta$ is the Kronecker symbol.

Let us denote the vector $U^{\ell,m}$ made of values $u_j^{\ell,m}$. This vector solves the following linear system :

$$(-\omega^2 M_h + K_h^\ell)U^{\ell,m} = F^{\ell,m}$$

with the mass matrix $M_h$ :

$$(M_h)_{i,j} \;=\; \oint_0^R \widetilde{\rho}\, r^2\, \varphi_j\, \varphi_i\, dr$$

and the stiffness matrix $K_h$ (with absorbing boundary condition)

$$(K_h^\ell)_{i,j} \;=\; \oint_0^R \widetilde{\mu}\, r^2 \frac{\partial \varphi_j}{\partial r} \frac{\partial \varphi_i}{\partial r}\, dr \;+\; \ell(\ell+1) \oint_0^R \widetilde{\mu}\, \varphi_j\, \varphi_i\, dr - ik(\omega)\, \widetilde{\mu}\, R^2\, \varphi_j(R)\, \varphi_i(R)$$

Gauss-Lobatto points achieve mass lumping, i.e. the mass matrix $M_h$ is diagonal. It can also be noticed that the $\ell(\ell+1)$ term in the stiffness matrix is a diagonal matrix. The right hand side $F^{\ell,m}$ is made of components $f_i^{\ell,m}$.

## 2.3 Validation for the scattering by a plane wave

We consider $N$ spherical layers, with $\widetilde{\rho}$ and $\widetilde{\mu}$ constant on each layer :

$$(\widetilde{\rho}(x), \widetilde{\mu}(x)) = (\widetilde{\rho}_i, \widetilde{\mu}_i), \quad r_i \le x \le r_{i+1}$$

The radii $(r_i)_{0 \le i \le N}$ are increasing :

$$r_0 < r_1 < r_2 \cdots r_{N-1} < r_N$$

Analytical solutions for the case of an incident plane wave can be computed by using spherical Bessel functions (see Appendix A). The following parameters are chosen with an absorbing boundary condition set at $r_3 = 2$:

$$\omega \;=\; 4\pi, \quad r_0 \;=\; 0, \quad r_1 \;=\; 0.7, \quad r_2 \;=\; 1.0, \quad r_3 \;=\; 2.0$$

$$\widetilde{\rho}_0 = 0.8, \quad \widetilde{\rho}_1 = 0.2, \quad \widetilde{\rho}_2 = 1.0$$

$$\widetilde{\mu}_0 = 1.5, \quad \widetilde{\mu}_1 = 2.0, \quad \widetilde{\mu}_2 = 1.0$$

The solution is plotted in figure 1. The computation of this analytical solution is performed in multiple precision (with the library MPFR) such that all the 16 digits of the reference solution are exact. In figure 2, the relative $L^2$ error between the reference solution and the numerical solution is represented versus $\dfrac{h}{r}$ where h is the mesh size for different orders of approximation. This relative $L^2$ error is computed on the (x,z) plane $[-2,2] \times \{0\} \times [-2,2]$ with $200 \times 200$ points. The numerical solution is computed in double precision, therefore we observe that the $L^2$ error does not go below $10^{-13}$, which is satisfying. Since the quantity $h/r$ is related to the number of degrees of freedom, it is easy to see that higher accuracy is obtained when using higher order of approximations for a same number of degrees of freedom. The direction of the plane wave has been chosen equal to $e_y$ such that all modes $m$ are excited (and not only the mode $m = 0$). The figure shows that the convergence of the finite element is optimal in $O(h^{r+1})$ for this type of source. The degree of harmonical spherics $L$ is chosen automatically such that

$$||u^{\ell,m}||_\infty \le \varepsilon, \quad \forall \ell, |m| > L + 1$$

We have chosen $\varepsilon = 10^{-15}$, it has been observed that we obtained $L \le 40$, and that the convergence is exponential in $L$ as expected.

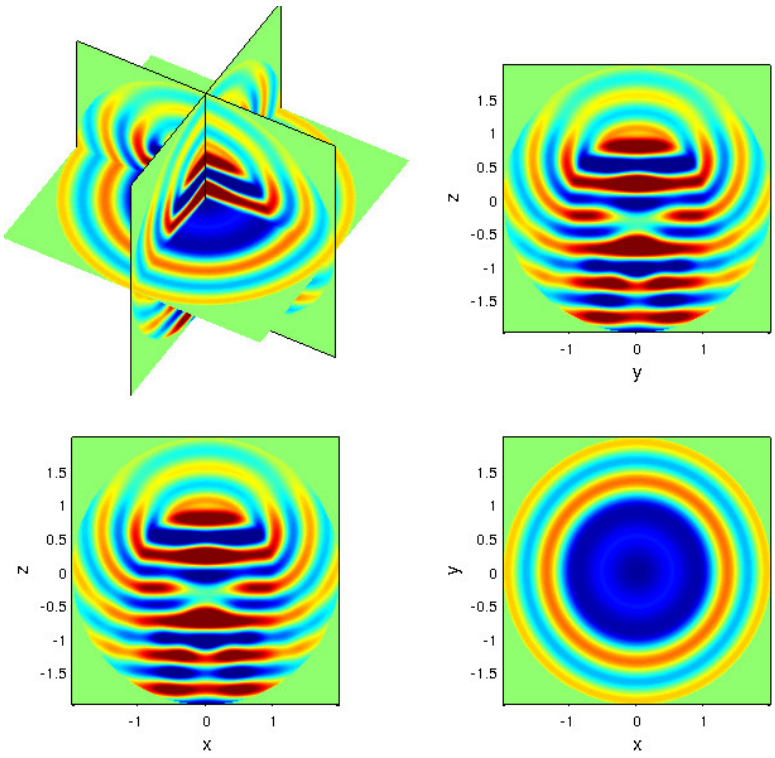


Figure 1: Real part of the solution for the scattering of spherical layers.

## 2.4 Numerical Green's function

The Green's function for Helmholtz equation is equal to:

$$G(x,y) = \frac{e^{ik|x-y|}}{4\pi|x-y|}$$

where $k$ is the wave number. In this subsection, we choose an homogeneous medium with

$$\widetilde{\rho} = \widetilde{\mu} = 1,\ \omega = 4\pi,\ R = 4$$

A transparent condition is set on the outer sphere:

$$\frac{\partial u^{\ell,m}}{\partial r} = \frac{k h_\ell^{(1)'}(kR)}{h_\ell^{(1)}(kR)}\, u^{\ell,m}$$

where $h_\ell^{(1)}$ is the spherical Hankel function of first kind as introduced in the appendix A. The numerical Green's function is computed by selecting a Dirac for the source $f$:

$$f = \delta_{x=y}$$

where $y$ is the point source (the second argument of the Green's function). We have the following discrete right hand side:

$$F_i^{\ell,m} = \begin{cases} \dfrac{1}{4\pi}\varphi_i(0)\,\delta_{\ell,0}\,\delta_{m,0} \ \text{ if } \ y = (0,0,0) \\ \varphi_i(r_s)\,\bar{Y}_\ell^m(\theta_s,\phi_s) \ \text{ where } (r_s,\theta_s,\phi_s) \text{ are the spherical coordinates of } y \end{cases}$$

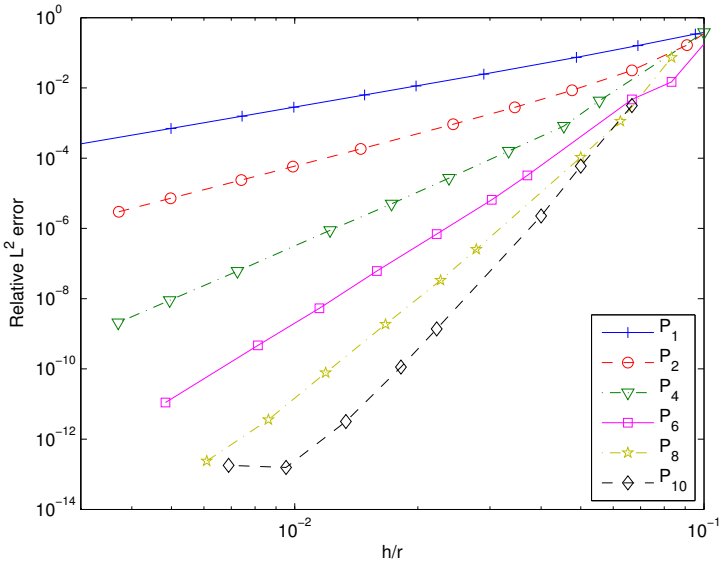


Figure 2: Relative $L^2$ error obtained using 1-D finite elements (radial symmetry) versus $h/r$ for the scattering of spherical layers. Different order of approximations are considered.

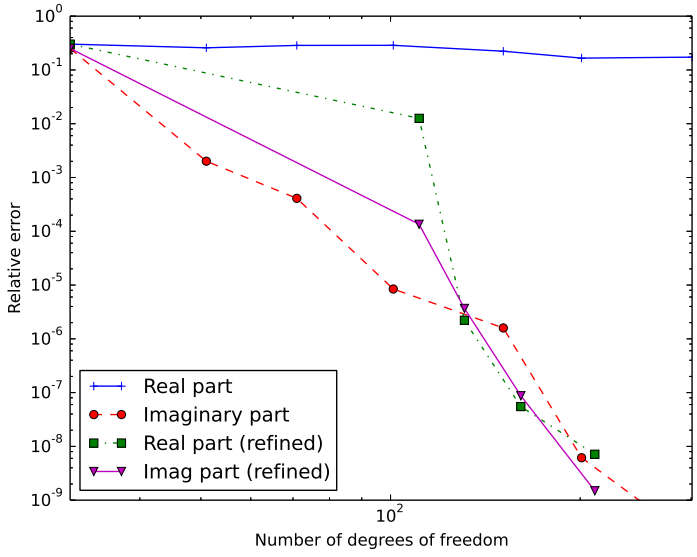


Figure 3: Relative $L^2$ error versus the number of degrees of freedom for the real part or imaginary part of Green's function. The point source is the center (0,0,0), a local refinement is performed or not.

When the point source $y$ is located on the center, only the mode $m = \ell = 0$ is involved. In figure 3, we have represented the $L^2$ error between the numerical Green's function and the analytical Green's function when $y = (0, 0, 0)$. This error is computed with 10000 points in the interval $r \in [0.01, 4]$ for tenth-order finite elements. When a local refinement is performed on the center, both real part and imaginary part are converging fastly towards the exact solution. When the mesh is uniform, only the imaginary part exhibits a fast convergence. This can be explained because the real part of the Green's function is singular whereas the imaginary part is regular. When the point source $y$ is located on the axis Oz, only modes with $m = 0$ are involved.

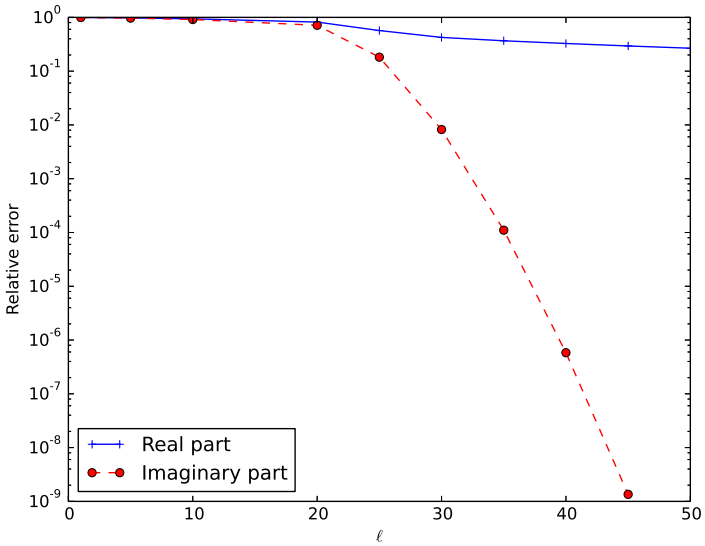


Figure 4: Relative $L^2$ error versus the number of modes $L$ for the real part or imaginary part of Green's function. The point source is the point (0,0,2), a local refinement is performed in $r$.

For $y = (0, 0, 2)$, a 1-D mesh is constructed with a local refinement close to the vertex $r = 2$. Then, the numerical error is observed versus the number of modes $L$ ($\ell = 0..L$) for $200 \times 200$ points on the plane $[-4, 4] \times \{0\} \times [-4, 4]$ (see figure 4). Again, the imaginary part is correctly computed (with an exponential convergence with respect to $L$), whereas the real part would require a very large number of modes to be accurate enough (especially close to the source point $y$). This is logical since the use of spherical harmonics in $\theta, \phi$ prevents us from applying a local refinement in $\theta, \phi$, as it would have been possible in a 3-D mesh for instance.

# 3 Solution with axial symetry (2.5D)

In this section, cylindrical coordinates $(r, \theta, z)$ are used :

$$\begin{cases} x = r\cos\theta \\ y = r\sin\theta \\ z = z \end{cases}$$

It can be noticed that the present angle $\theta$ corresponds to the previous angle $\phi$ of spherical coordinates. The computational domain $\Omega$ is the generating section of the geometry, i.e. the half-disk of radius $R$ in the case of the sphere. This computational domain is meshed in quadrilateral elements.

$$\Omega \;=\; \bigcup_{i=1}^{N_e} K_i$$

Compared to radial symmetry, the physical coefficients $\widetilde{\rho}$, $\widetilde{\mu}$, $\widetilde{M}$ and $\widetilde{\beta}$ and the geometry may depend on $r$ and $z$ and are assumed to not depend on the variable $\theta$. Spectral approximation is used in $\theta$ since the fields are $2\pi$-periodic. Such a choice leads to a sequence of decoupled 2-D problems to solve. In time domain, $u$ would be searched with sine and cosine expansions:

$$u(r,\theta,z) \;=\; \sum_{m=0}^{\infty} u^{m,c}(r,z)\,\cos(m\theta) \;+\; \sum_{m=1}^{\infty} u^{m,s}(r,z)\,\sin(m\theta)$$

In time-harmonic domain, since $u$ is complex, the Fourier expansion is used:

$$u(r,\theta,z) \;=\; \sum_{m=-\infty}^{\infty} u^m e^{-im\theta}$$

The mode $m$ of $u$ is searched with 2-D basis functions generating the discrete space $V_h$:

$$u^m = \sum_{j=0}^{N_h} u_j^m\,\varphi_j(r,z)$$

where $N_h$ is the number of degrees of freedom of the 2-D mesh. In cylindrical coordinates the laplacian is given as

$$\mathrm{div}\,(\widetilde{\mu}\nabla u) = \frac{1}{r}\frac{\partial}{\partial r}\left(\widetilde{\mu}\,r\,\frac{\partial u}{\partial r}\right) + \frac{\widetilde{\mu}}{r^2}\,\frac{\partial^2 u}{\partial\theta^2} + \frac{\partial}{\partial z}\left(\widetilde{\mu}\frac{\partial u}{\partial z}\right)$$

As a result, each mode $u^m$ solves the following equation

$$\begin{aligned}
&-\omega^2\widetilde{\rho}\,u^m - 2i\omega\left(\widetilde{M}_r\frac{\partial u}{\partial r} - \frac{im\widetilde{M}_\theta}{r}u + \widetilde{M}_z\frac{\partial u}{\partial z}\right) + \widetilde{M}_r\frac{\partial}{\partial r}\left[\widetilde{\beta}\left(\widetilde{M}_r\frac{\partial u}{\partial r} - \frac{im\widetilde{M}_\theta}{r}u + \widetilde{M}_z\frac{\partial u}{\partial z}\right)\right]\\
&-\frac{im\widetilde{M}_\theta}{r}\left[\widetilde{\beta}\left(\widetilde{M}_r\frac{\partial u}{\partial r} - \frac{im\widetilde{M}_\theta}{r}u + \widetilde{M}_z\frac{\partial u}{\partial z}\right)\right] + \widetilde{M}_z\frac{\partial}{\partial z}\left[\widetilde{\beta}\left(\widetilde{M}_r\frac{\partial u}{\partial r} - \frac{im\widetilde{M}_\theta}{r}u + \widetilde{M}_z\frac{\partial u}{\partial z}\right)\right]\\
&-\frac{1}{r}\frac{\partial}{\partial r}\left(\widetilde{\mu}\,r\,\frac{\partial u^m}{\partial r}\right) + \frac{\widetilde{\mu}\,m^2}{r^2}u^m - \frac{\partial}{\partial z}\left(\frac{\widetilde{\mu}\partial u^m}{\partial z}\right) = f^m
\end{aligned} \tag{3}$$

The variational formulation can be obtained from the 3-D formulation (2) by taking

$$v = \varphi_i(r,z)e^{-im\theta}$$

Hence we obtain for each mode $u^m$: Find $u^m \in V_h$ such that for all $\phi_i \in V_h$,

$$\begin{aligned}
&-\omega^2\int_\Omega r\,\widetilde{\rho}\,u^m\,\varphi_i\,dx - i\omega\int_\Omega r\widetilde{B}\cdot\nabla u^m\varphi_i\,dx + i\omega\int_\Omega r\widetilde{B}\cdot\nabla\varphi_i\,u^m\,dx\\
&+\int_\Omega r\,\widetilde{C}\nabla u^m\cdot\nabla\varphi_i\,dx + m^2\int_\Omega\frac{\widetilde{A}}{r}u^m\varphi_i\,dx - \int_\Gamma r\,\widetilde{\mu}\frac{\partial u^m}{\partial n}\,\varphi_i\,dx = f_i^m
\end{aligned} \tag{4}$$

with the following coefficients

$$\widetilde{A} = \widetilde{\mu}_{\theta,\theta} - \widetilde{\beta}\widetilde{M}_\theta^2 - \frac{2r\,\omega\widetilde{M}_\theta}{m}$$

$$\widetilde{B} = \begin{bmatrix} \widetilde{M}_r + \dfrac{m\widetilde{\beta}\,\widetilde{M}_\theta\widetilde{M}_r}{r\,\omega} \\ \widetilde{M}_z + \dfrac{m\widetilde{\beta}\,\widetilde{M}_\theta\widetilde{M}_z}{r\,\omega} \end{bmatrix}$$

$$\widetilde{C} = \begin{pmatrix} \widetilde{\mu}_{r,r} - \widetilde{\beta}\widetilde{M}_r^2 & \widetilde{\mu}_{r,z} - \widetilde{\beta}\widetilde{M}_r\widetilde{M}_z \\ \widetilde{\mu}_{r,z} - \widetilde{\beta}\widetilde{M}_r\widetilde{M}_z & \widetilde{\mu}_{z,z} - \widetilde{\beta}\widetilde{M}_z^2 \end{pmatrix}$$

Here we have considered an anisotropic tensor $\widetilde{\mu}$ with $\widetilde{\mu}_{r,\theta} = \widetilde{\mu}_{z,\theta} = 0$. The source term is given as:

$$f_i^m = \frac{1}{2\pi}\int_\Omega \int_0^{2\pi} r f(r,\theta,z)\varphi_i(r,z)e^{im\theta}\,d\theta dr\,dz$$

### 3.1 2-D finite elements

Let us denote $F_i$ the transformation from the unit square $\hat{K}$ to the real element $K_i$ (see figure 5). For $m = 0$, $u^m$ is searched in the following finite element space:

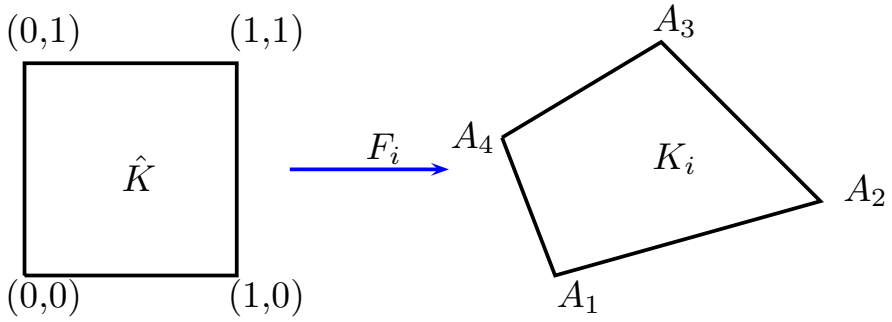


Figure 5: Transformation $F_i$ for a quadrilateral.

$$V_h \;=\; \left\{u \in H^1(\Omega) \text{ such that } u|_{K_i} \circ F_i \in \mathbb{Q}_r\right\}$$

where

$$\mathbb{Q}_r \;=\; \text{Span}\left\{\hat{x}^i\hat{y}^j, \quad 1 \le i,j \le r+1\right\}$$

$r$ is the order of approximation. The integrals involved in the variational formulation are regular since $m = 0$. The basis functions on the reference element $\hat{K}$ are products of 1-D basis functions for the unit square :

$$\hat{\varphi}_i(\hat{x},\hat{y}) = \hat{\varphi}_{i_1}^{GL}(\hat{x})\hat{\varphi}_{i_2}^{GL}(\hat{y})$$

where the 1-D basis functions $\hat{\varphi}_i^{GL}$ are based on Gauss-Lobatto points as explained in the previous section. The integrals can also be evaluated with the same Gauss-Lobatto points leading to faster

computations. The basis functions on the real element are given by the relation

$$\hat{\varphi}_j = \varphi_j \circ F_i$$

For $m \neq 0$, $u^m$ is searched in the following finite element space

$$V_h^0 \;=\; \left\{ u \in H^1(\Omega) \text{ such that } u = 0 \text{ for } r = 0, \text{ and } u|_{K_i} \circ F_i \in \mathbb{Q}_r \right\}$$

Because of the homogeneous Dirichlet condition on the axis, the integrals are well-defined.

The vector $U^m$ solves the following linear system:

$$A_h^m U^m = F^m$$

with the finite element matrix $A_h^m$ (with a first-order absorbing boundary condition):

$$\begin{aligned}(A_h^m)_{i,j} \;=\; & -\omega^2 \int_\Omega r\,\widetilde{\rho}\,\varphi_j\,\varphi_i\,dx - i\omega \int_\Omega r\widetilde{B}\cdot\nabla\varphi_j\varphi_i\,dx + i\omega \int_\Omega r\widetilde{B}\cdot\nabla\varphi_i\,\varphi_j\,dx \\ & + \int_\Omega r\,\widetilde{C}\nabla\varphi_j\cdot\nabla\varphi_i\,dx + m^2\int_\Omega \frac{\widetilde{A}}{r}\varphi_j\varphi_i\,dx - \int_\Gamma ir\widetilde{\mu}\,k(\omega)\varphi_j\varphi_i\,dx\end{aligned}$$

where $\Gamma$ is the boundary of $\Omega$ (i.e. the half circle of radius $R$ for the sphere).

## 3.2 Validation for the scattering by a plane wave

We consider the scattering of spherical layers, with the same parameters as in the subsection 2.3. The plane wave is written in cylindrical coordinates:

$$e^{i\vec{k}\cdot x} = e^{ik_z z} e^{ik_\perp r cos(\theta-\theta_0)}$$

where

$$k_\perp = \sqrt{k_x^2 + k_y^2}, \quad (\cos\theta_0, \sin\theta_0) = \frac{(k_x, k_y)}{k_\perp}$$

The decomposition of this plane wave in Fourier series is achieved by using Jacobi-Anger expansion:

$$e^{i\vec{k}\cdot x} = e^{ik_z z} \sum_{m=-\infty}^{\infty} (-i)^m J_m\left(k_\perp r\right) e^{-im(\theta-\theta_0)}$$

This expression is used to compute the right hand side coefficients $f_i^m$ without using quadrature rules. A non-axial incidence is selected (actually the wave vector $\vec{k}$ is oriented about $e_y$) such that all the modes are excited, and not only the mode $m = 0$. An example of quadrilateral mesh used for the computations can be seen in figure 6. In figure 7, the relative $L^2$ error between the reference solution and the numerical solution is displayed. This relative $L^2$ error is computed on the (x,z) plane $[-2, 2] \times 0 \times [-2, 2]$ with $200 \times 200$ points. An optimal convergence in $O(h^{r+1})$ is obtained as expected, and a spectral accuracy in $m$. 75 modes are sufficient to obtain a machine precision accuracy ($-37 \leq m \leq 37$).

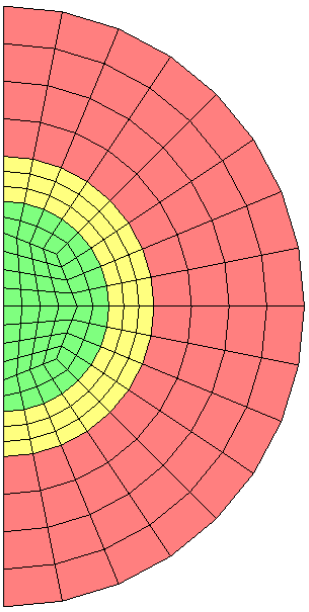

Figure 6: Example of quadrilateral mesh used to compute the solution for the scattering of spherical layers.

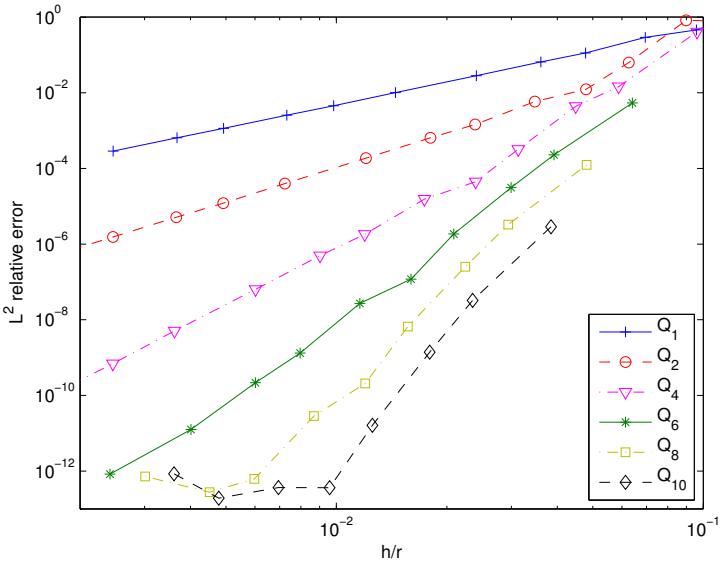


Figure 7: Relative $L^2$ error versus $h/r$ for non-axial incidence. Different order of approximations are considered, Gauss-Lobatto quadrature rules are used.

### 3.3 Formulation $R_3$

In Eq. (4), the integral containing the fraction $\frac{1}{r}$ will not be evaluated exactly by using Gauss-Legendre quadrature formulae. Moreover, we could expect that for small elements close to the axis, the numerical error due to the non-exactness of quadrature rules, might increase. In order to achieve an exact integration, we can search $u$, $\varphi$ as:

$$u^m = r\tilde{u}, \quad \varphi = r\tilde{\varphi}$$

and obtain the following variational formulation (called $R_3$): Find $\tilde{u} \in V_h$ such that for all $\tilde{\varphi} \in V_h$,

$$\begin{aligned} -\omega^2 \int_\Omega r^3\, \widetilde{\rho}\, \tilde{u}\, \tilde{\varphi}_i \, dx - i\omega \int_\Omega r^2 \widetilde{B} \cdot \nabla\left(r\tilde{u}\right) \tilde{\varphi}_i \, dx + i\omega \int_\Omega r^2 \widetilde{B} \cdot \nabla\left(r\tilde{\varphi}_i\right) \tilde{u}\, dx \\ + \int_\Omega r\, \widetilde{C} \nabla\left(r\tilde{u}\right) \cdot \nabla\left(r\tilde{\varphi}_i\right) \, dx + m^2 \int_\Omega r \widetilde{A} \tilde{u} \tilde{\varphi}_i \, dx - \int_\Gamma r^2\, \widetilde{\mu} \frac{\partial\left(r\tilde{u}\right)}{\partial n} \tilde{\varphi}_i \, dx = f_i^m \end{aligned} \tag{5}$$

The usual formulation and the formulation $R_3$ are compared for elongated bodies. A first case is the scattering of an ellipsoide (see figure 8). A Dirichlet condition is set on the surface of

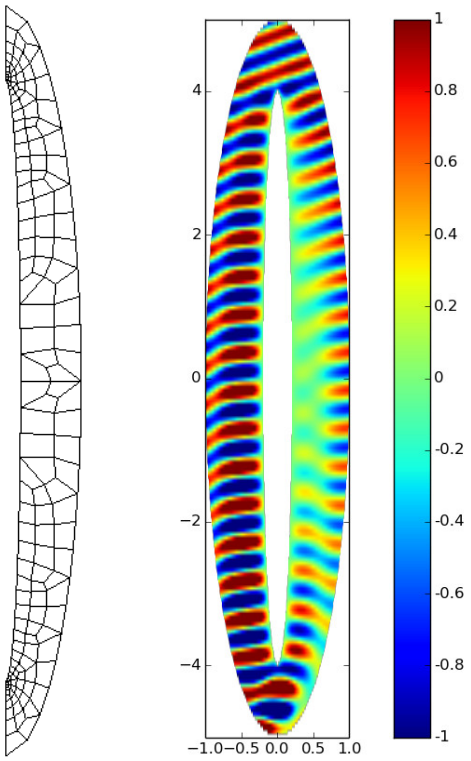


Figure 8: On the left, mesh used to computed the scattering of an ellipsoide. On the right, real part of the total field on the plane Oxz.

the ellipsoide of axis $a = 0.2, b = 4.0$. The parameters of the problem are the following ones:

$$\vec{u} = \left(\sin 160^\circ, 0, \cos 160^\circ\right), \ \omega = 4\pi$$

Because of the high curvature close to the point $(0, 0, b)$, the mesh is finer close to this point. The two formulations converge with the optimal order as shown in figure 9, but the formulation $R_3$ is less accurate. The reference solution is computed on a finer mesh with $\mathbb{Q}_{10}$ approximation, the solutions are compared on the three planes Oxy, Oxz, Oyz with $200 \times 200$ points on each plane. The integrals are here evaluated with Gauss-Legendre rules (which are exact for $\mathbb{Q}_{2r+1}$) for both formulations.

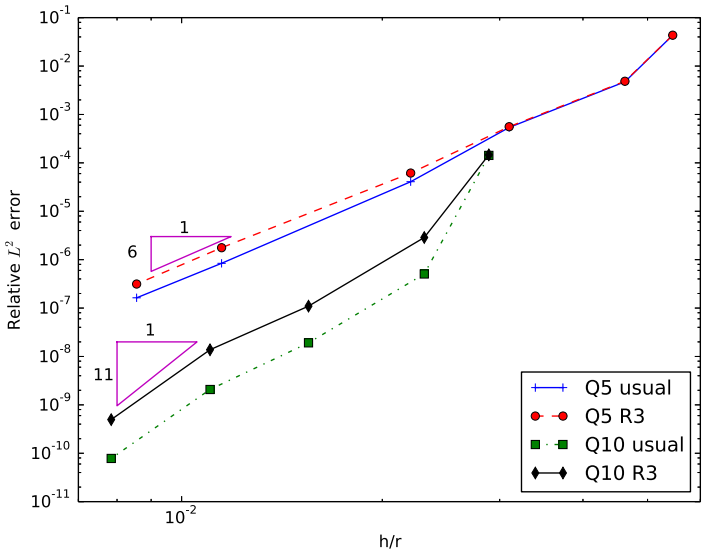


Figure 9: Relative $L^2$ error versus $h/r$ for $\mathbb{Q}_5$ and $\mathbb{Q}_{10}$ and two formulations. Case of the ellipsoide, Gauss-Legendre rules are used.

A second case is the scattering of a cone-sphere (see figure 10). The radius of the sphere is equal to 0.1, and the angle of the cone is 12.5°. A local refinement is performed in the vicinity of the tip in order to capture correctly the singularity. The parameters of the problem are the following ones:

$$\vec{u} = (\sin 160°, 0, \cos 160°)\,,\ \omega = 20\pi$$

As for the ellipsoide, the reference solution is computed on a finer mesh, and the solutions are compared on the three planes Oxy, Oxz and Oyz. In figure 11, the relative $L^2$ errors are displayed for the two formulations. The convergence is here less nice than for the ellipsoide, but the formulation $R_3$ is also less accurate for this case. It seems clear to us that the usual formulation is more accurate and simpler to implement than the formulation $R_3$. As a result, in the sequel, only the usual formulation will be considered.

## 3.4 Mass lumping and quadrature rules

In time-domain, for a null flow ($\widetilde{M} = 0$), the evolution system reads

$$M_h \frac{d^2U}{dt^2} + K_h U = F_h$$

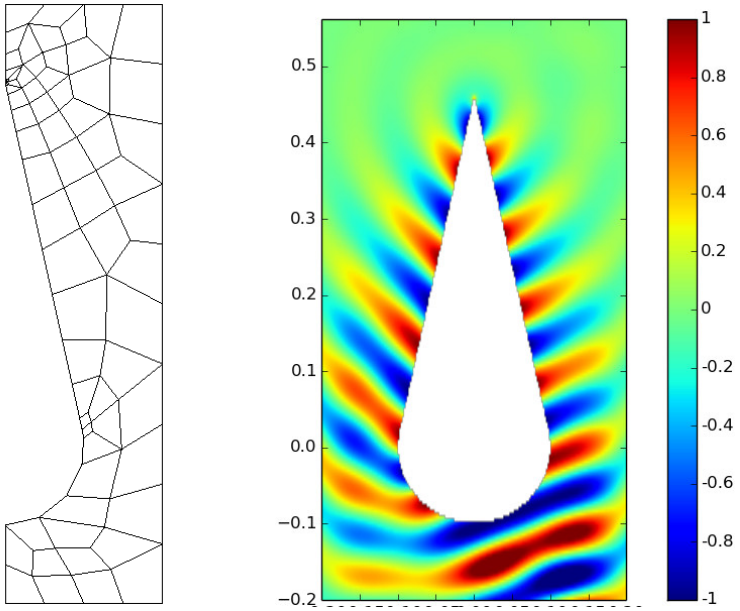


Figure 10: On the left, mesh used to computed the scattering of a cone-sphere. On the right, real part of the total field on the plane Oxz.

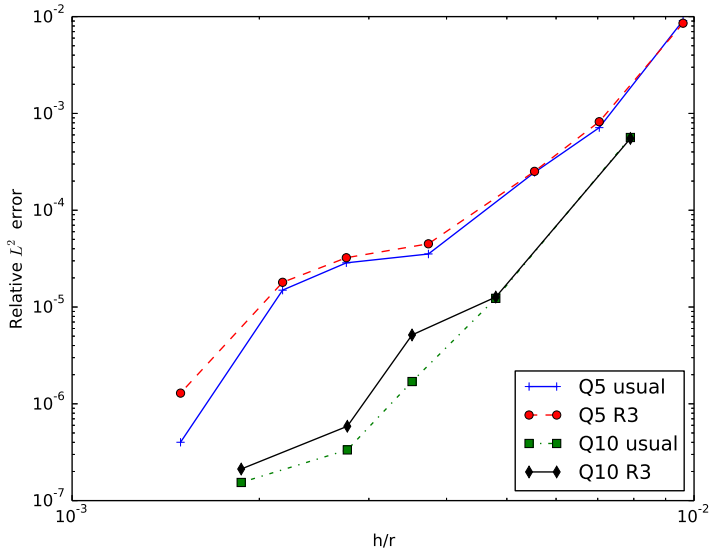


Figure 11: Relative $L^2$ error versus $h/r$ for $\mathbb{Q}_5$ and $\mathbb{Q}_{10}$ and two formulations. Case of the cone-sphere.

The mass matrix $M_h$ is given as

$$(M_h)_{i,j} = \int_\Omega r\,\widetilde{\rho}\,\varphi_j\,\varphi_i\,dx$$

The stiffness matrix $K_h$ is given as

$$(K_h)_{i,j} = \int_\Omega r\,\widetilde{\mu}\,\frac{\partial\varphi_j}{\partial r}\frac{\partial\varphi_i}{\partial r}\,dx + m^2\int_\Omega \frac{\widetilde{\mu}}{r}\varphi_j\,\varphi_i\,dx + \int_\Omega r\,\widetilde{\mu}\,\frac{\partial\varphi_j}{\partial z}\frac{\partial\varphi_i}{\partial z}\,dx$$

For a non-null flow, the expressions are more complex, and the evolution system can be written under the form

$$M_h\frac{d^2U}{dt^2} + S_h\frac{dU}{dt} + K_hU = F_h$$

Explicit time-stepping is feasible if the mass matrix $M_h$ is diagonal and invertible. When $m \neq 0$, a Dirichlet condition is set on degrees of freedom located on the axis, such that these degrees of freedom are no longer in the evolution system. As a result, Gauss-Lobatto points can be used to achieve mass lumping.

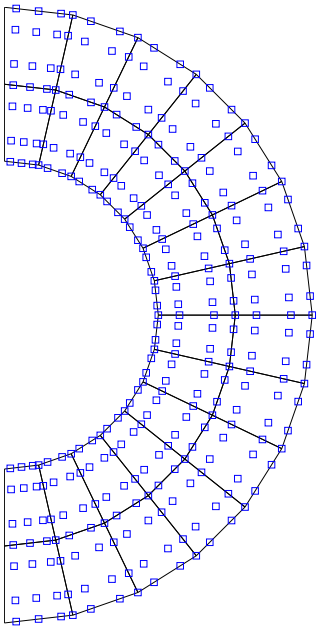

Figure 12: Degrees of freedom on a circular mesh, with Gauss-Radau points for elements on the axis, and Gauss-Lobatto points elsewhere

When $m$ is equal to 0, the degrees of freedom on the axis cannot be eliminated from the evolution system. If Gauss-Lobatto points are used as quadrature points, the mass matrix $M_h$ is diagonal but the entries associated with degrees of freedom located on the axis are null and therefore $M_h$ is no longer invertible. A first solution is to consider a Discontinuous Galerkin formulation, such that Gauss points (on elements close to the axis, or for all the elements) can be used instead of Gauss-Lobatto points. Here, we propose a second solution which consists of using Gauss-Radau points for elements adjacent to the axis (an edge of the element belongs

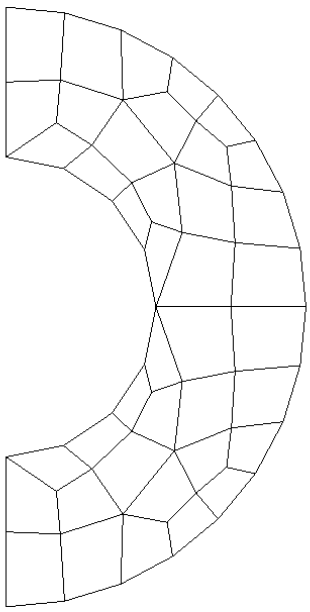

Figure 13: Mesh where mass lumping can not be achieved.

to the axis). Gauss-Radau points are quadrature points exact for $\mathbb{Q}_{2r}$ including only the right extremity of the interval $[0, 1]$ (whereas Gauss-Lobatto points include the two extremities). In figure 12, the degrees of freedom are displayed when Gauss-Radau points are used for elements on the axis, and Gauss-Lobatto points elsewhere. This procedure provides a diagonal mass matrix, which is invertible (since there is no degree of freedom located on the axis).

However, choosing these particular degrees of freedom is not always possible. All the quadrilaterals that touch the axis must have an edge on the axis. For example, the mesh represented in figure 13 is not compliant.

For the scattering of spherical layers, we observe (cf. figure 14) that the accuracy obtained with Gauss-Radau points is almost the same as with Gauss-Lobatto points and similar to classical Gauss-Legendre rules. In the sequel, we will use Gauss-Lobatto rules only, since they are more efficient. Since we are interested in time-harmonic simulations, the non-invertibility of the mass matrix is not an issue since the global finite element matrix $A_h^m$ is invertible .

## 3.5 Cylindrical Perfectly Matched Layers

The PML are introduced by a complex variable change:

$$\begin{cases} \tilde{r} \;=\; r + \dfrac{i}{\omega} \displaystyle\int_{r_0}^{r} \sigma_r(s)\, ds \\ \tilde{z} \;=\; z + \dfrac{i}{\omega} \displaystyle\int_{z_0}^{z} \sigma_z(s)\, ds \end{cases}$$

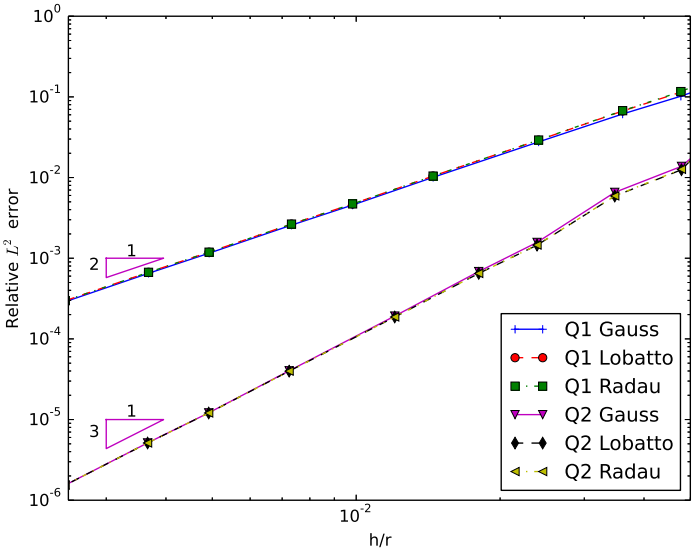


Figure 14: Relative $L^2$ error for different quadrature rules (Gauss, Gauss-Radau and Gauss-Lobatto) for $\mathbb{Q}_1$ and $\mathbb{Q}_2$ and the scattering of spherical layers

where $r_0, z_0$ are associated with the beginning of PML layers. The damping functions are the classical parabolic functions (see [7]):

$$\sigma_r(s) = \sigma \frac{3\log(1000)\, v_{\max}}{2a^3}(s - r_0)^2$$

where $v_{\max}$ is the maximal velocity of waves in PML layers, $a$ the thickness of the layer and $\sigma$ a damping coefficient. The original equations are transformed by substituting $(r, z)$ with $(\tilde{r}, \tilde{z})$, derivatives are transformed back in variables $r, z$ by using the chain rule :

$$\frac{\partial}{\partial \tilde{r}} = \frac{dr}{d\tilde{r}}\frac{\partial}{\partial r} = \frac{1}{\tau_r}\frac{\partial}{\partial r}$$

$$\frac{\partial}{\partial \tilde{z}} = \frac{dz}{d\tilde{z}}\frac{\partial}{\partial z} = \frac{1}{\tau_z}\frac{\partial}{\partial z}$$

where coefficients $\tau_r, \tau_z$ are given as

$$\tau_r = 1 + \frac{i\sigma_r}{\omega}$$

$$\tau_z = 1 + \frac{i\sigma_z}{\omega}$$

By multiplying with $\tilde{r}\,\tau_r\,\tau_z\varphi$, the variational formulation is given as

$$-\omega^2 \int_\Omega \tilde{r}\,\tilde{\rho}\,\tau_r\,\tau_z\,u\,\varphi\,dx \; - i\omega \int_\Omega \tilde{r} \begin{bmatrix} \widetilde{B}_r\tau_z \\ \widetilde{B}_z\tau_r \end{bmatrix} \cdot \nabla u\,\varphi\,dx + i\omega \int_\Omega \tilde{r} \begin{bmatrix} \widetilde{B}_r\tau_z \\ \widetilde{B}_z\tau_r \end{bmatrix} \cdot \nabla\varphi\,u\,dx$$

$$+ \int_\Omega \tilde{r} \begin{bmatrix} \widetilde{C}_{r,r}\dfrac{\tau_z}{\tau_r} & 0 \\ 0 & \widetilde{C}_{z,z}\dfrac{\tau_r}{\tau_z} \end{bmatrix} + m^2 \int_\Omega \frac{\widetilde{A}}{\tilde{r}}\,\tau_r\,\tau_z\,u\,\varphi\,dx = \int_\Omega \tilde{r}\tau_r\tau_z f^m \varphi\,dx$$

where the coefficients $\widetilde{A}, \widetilde{B}, \widetilde{C}$ are modified by replacing $r$ with $\tilde{r}$. The tensor $\widetilde{C}$ is assumed to be orthotropic, since an anisotropic tensor should cause a problem with the classical PMLs devised here. The numerical Green's function is plotted in figure 15 with the following parameters:

$$\widetilde{\rho} = \widetilde{\mu} = 1,\ \widetilde{M} = (0, 0, 0.5),\ \widetilde{\beta} = 1,\ \omega = 4\pi$$

With these parameters, the flow is aligned with the axis of the PML layers. The thickness of the

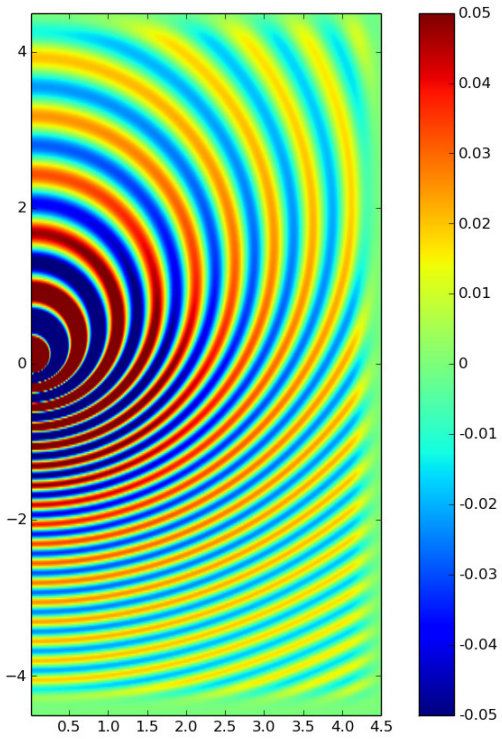


Figure 15: Imaginary part of the numerical Green's function with cylindrical PMLs (PMLs areas are represented, $\sigma = 1$). Case of an uniform flow $\widetilde{M}_z = 0.5, \widetilde{\beta} = 1$

PML will always be chosen equal to the wavelength. The convergence of the numerical Green's function is displayed in figure 18.

## 3.6 Spherical Perfectly Matched Layers

As opposed to the previously presented PML which were designed for a cylindrical geometry, the following ones are designed to match the boundary of a spherical geometry as a sphere. We assume here that $\widetilde{\mu}$ is isotropic and that $\widetilde{\beta} = 0$. The PML are introduced by a complex variable change in the spherical variable $r_{\text{sph}}$ only. So first we rewrite the equations into spherical

coordinates $(\tilde{r}_{\text{sph}}, \psi, \theta)$ :

$$-\omega^2\widetilde{\rho}u - 2\frac{m}{\tilde{r}_{\text{sph}}\sin\psi}\,\omega\,\widetilde{M}_\theta\,u - 2i\omega\left(\widetilde{M}_{r_{\text{sph}}}\frac{\partial u}{\partial\tilde{r}_{\text{sph}}} + \frac{\widetilde{M}_\psi}{\tilde{r}_{\text{sph}}}\frac{\partial u}{\partial\psi}\right)$$
$$-\frac{1}{\tilde{r}^2_{\text{sph}}}\frac{\partial}{\partial\tilde{r}_{\text{sph}}}\left(\widetilde{\mu}\,\tilde{r}^2_{\text{sph}}\,\frac{\partial u}{\partial\tilde{r}_{\text{sph}}}\right) + \frac{m^2\,\widetilde{\mu}}{\tilde{r}^2_{\text{sph}}\sin^2\psi}u - \frac{1}{\tilde{r}^2_{\text{sph}}\sin\psi}\frac{\partial}{\partial\psi}\left(\widetilde{\mu}\,\sin\psi\,\frac{\partial u}{\partial\psi}\right) = f$$

where

$$\widetilde{M}_{r_{\text{sph}}} = \widetilde{M}_r\sin\psi + \widetilde{M}_z\cos\psi, \quad \widetilde{M}_\psi = \widetilde{M}_r\cos\psi - \widetilde{M}_z\sin\psi$$

Then we make the following change of variable:

$$\widetilde{r}_{\text{sph}} \;=\; r_{\text{sph}} + \frac{i}{\omega}\int_{r_0}^{r_{\text{sph}}}\sigma_r(s)\,ds$$

The derivatives are transformed back in physical variables $(r_{\text{sph}}, \psi, \theta)$ with the relation

$$\frac{\partial}{\partial\tilde{r}_{\text{sph}}} = \frac{1}{\tau_r}\frac{\partial}{\partial r_{\text{sph}}}$$

where

$$\tau_r = 1 + i\frac{\sigma_r}{\omega}$$

The equation is multiplied by $\tilde{r}^2_{\text{sph}}\sin\psi\,\tau_r\,\varphi$ to obtain the variational formulation:

$$-\omega^2\int_\Omega\widetilde{\rho}\,\tau_r\,\tilde{r}^2_{\text{sph}}\sin\psi\,u\,\varphi\,dx$$
$$-2m\,\omega\int_\Omega\tilde{r}_{\text{sph}}\,\tau_r\,\widetilde{M}_\theta\,u\,\varphi\,dx - 2i\omega\int_\Omega\tilde{r}^2_{\text{sph}}\sin\psi\widetilde{M}_{r_{\text{sph}}}\frac{\partial u}{\partial r_{\text{sph}}}\,\varphi + \tilde{r}_{\text{sph}}\sin\psi\,\tau_r\,\widetilde{M}_\psi\,\frac{\partial u}{\partial\psi}\,\varphi\,dx$$
$$+m^2\int_\Omega\frac{\widetilde{\mu}\,\tau_r}{\sin\psi}u\,\varphi\,dx + \int_\Omega\tilde{r}^2_{\text{sph}}\frac{\widetilde{\mu}\,\sin_\psi}{\tau_r}\frac{\partial u}{\partial r_{\text{sph}}}\frac{\partial\varphi}{\partial r_{\text{sph}}} + \tau_r\,\widetilde{\mu}\,\sin\psi\frac{\partial u}{\partial\psi}\frac{\partial\varphi}{\partial\psi}\,dx = \int_\Omega\tilde{r}^2_{\text{sph}}\sin\psi\,\tau_r\,f\,dx$$

And finally we come back into the cylindrical variables using the relation

$$\begin{cases} r = r_{\text{sph}}\sin\psi \\ z = r_{\text{sph}}\cos\psi \end{cases}$$

The chain rule provides the relations

$$\frac{\partial u}{\partial r_{\text{sph}}} = \sin\psi\frac{\partial u}{\partial r} + \cos\psi\frac{\partial u}{\partial z}, \quad \frac{\partial u}{\partial\psi} = r_{\text{sph}}\left(\cos\psi\frac{\partial u}{\partial r} - \sin\psi\frac{\partial u}{\partial z}\right)$$

The jacobian of the transformation from spherical coordinates $(r_{\text{sph}}, \psi, \theta)$ to cylindrical coordinates $(r, \theta, z)$ is equal to $-1/r_{\text{sph}}$. By applying these relations, we obtain the following

formulation:

$$
\begin{aligned}
-\omega^2 \int_\Omega \tilde{\rho}\, d\, \overline{d}\, \tilde{r}_{\text{sph}} \sin\psi\, u\, \varphi\, dx \; - 2\, m\, \omega \int_\Omega \widetilde{M}_\theta\, d\, \overline{d}\, u\, \varphi\, dx \\
- i\omega \int_\Omega \tilde{r}_{\text{sph}} \sin\psi \left( \hat{M}_r \left( \frac{\partial u}{\partial r}\varphi - \frac{\partial \varphi}{\partial r} u \right) + \hat{M}_z \left( \frac{\partial u}{\partial z}\varphi - \frac{\partial \varphi}{\partial z} u \right) \right) dx \\
+ \int_\Omega \widetilde{\mu}\, \tilde{r}_{\text{sph}} \sin\psi\, A\, \nabla u \cdot \nabla \varphi\, dx \; + \; m^2 \int_\Omega \widetilde{\mu}\, \frac{d\, \overline{d}}{\tilde{r}_{\text{sph}} \sin\psi} u\, \varphi\, dx \; = \int_\Omega d\, \overline{d}\, \tilde{r}_{\text{sph}} \sin\psi\, f\, \varphi\, dx
\end{aligned}
$$

where

$$
\begin{aligned}
\hat{M}_r &= \widetilde{M}_r \left( \overline{d} \sin^2\psi + d \cos^2\psi \right) + \widetilde{M}_z \cos\psi \sin\psi \left( \overline{d} - d \right) \\
\hat{M}_z &= \widetilde{M}_r \cos\psi \sin\psi \left( \overline{d} - d \right) + \widetilde{M}_z \left( \overline{d} \cos^2\psi + d \sin^2\psi \right)
\end{aligned}
$$

$$
\overline{d} = \frac{\widetilde{r}_{\text{sph}}}{r_{\text{sph}}} \quad d = \tau_r \qquad A = \begin{pmatrix} \dfrac{\overline{d}}{d}\sin^2\psi + \dfrac{d}{\overline{d}}\cos^2\psi & \left( \dfrac{\overline{d}}{d} - \dfrac{d}{\overline{d}} \right) \cos\psi \sin\psi \\ \left( \dfrac{\overline{d}}{d} - \dfrac{d}{\overline{d}} \right) \cos\psi \sin\psi & \dfrac{\overline{d}}{d}\cos^2\psi + \dfrac{d}{\overline{d}}\sin^2\psi \end{pmatrix}
$$

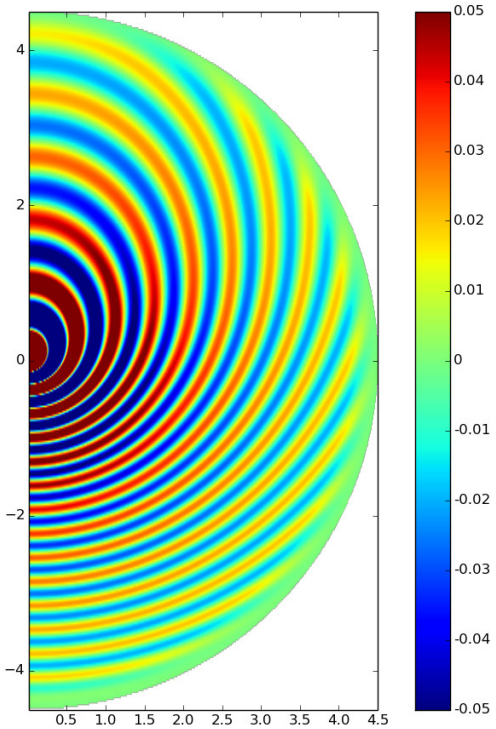


Figure 16: Imaginary part of the numerical Green's function with spherical PMLs (PMLs areas are represented, $\sigma = 1$). Case of an uniform flow $\widetilde{M}_z = 0.5,\ \widetilde{\beta} = 0$

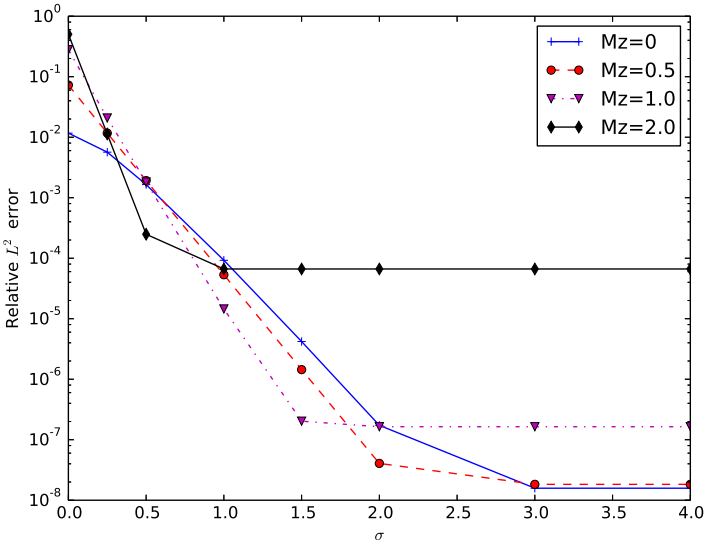


Figure 17: Relative $L^2$ error between the numerical Green's function and analytical one versus the damping coefficient $\sigma$. Spherical PML layers are used, case of an uniform flow with $\widetilde{\beta} = 0$ with different values of $\widetilde{M_z}$.

We retrieve a form very similar to [6], which is expected since the relation between cylindrical and spherical coordinates is similar to the relation between cartesian and polar coordinates in 2-D. It should be noted that inside the physical domain, we recover the variational formulation (4) because we have:

$$d = \overline{d} = 1, \quad \tilde{r}_{\text{sph}} \sin\psi = r_{\text{sph}} \sin\psi = r$$

inside the physical domain. The numerical Green's function is plotted in figure 16 with the following parameters:

$$\widetilde{\rho} = \widetilde{\mu} = 1, \ \widetilde{M} = (0, 0, 0.5), \ \widetilde{\beta} = 0, \ \omega = 4\pi$$

The convergence of the numerical Green's function is displayed in figure 17 with respect to the parameter $\sigma$. We observe that when the flow is increased, the $L^2$ relative error stagnates at higher levels. We are not sure if this problem comes from the strategy of the local refinement applied or from the PML layers. A good idea would be to compare with modified PML layers as proposed by [3].

## 3.7 Numerical Green's function

When $\widetilde{\beta} = 1$, the analytical Green's function is given as (see [4]):

$$G(x,y) = \frac{1}{4\pi|x-y|\sqrt{M_r^2+\beta^2}} e^{i\frac{k|x-y|}{\beta^2}\left(-M_r + \sqrt{M_r^2+\beta^2}\right)}$$

where

$$M_r = \frac{\widetilde{M}\cdot(x-y)}{|x-y|}, \ \beta = \sqrt{1-\widetilde{M}^2}$$

When $\widetilde{\beta} = 0$, the Green's function is given as:

$$G(x,y) = \frac{1}{4\pi|x-y|} e^{ik|x-y|\left(-M_r + \sqrt{1+\widetilde{M}^2}\right)}$$

The numerical Green's function is computed with a Dirac source. The discrete right hand side is given as:

$$f_i^m = \frac{1}{2\pi} \begin{cases} \varphi_i(y)\,\delta_{m,0} \text{ if } y \in Oz \\ \varphi_i(r_s,z_s)\,e^{im\theta_s} \text{ where } (r_s,\theta_s,z_s) \text{ are cylindrical coordinates of } y \end{cases}$$

The point-source $y$ is taken on the axis Oz since only the mode $m = 0$ is involved in this case. With the following parameters

$$\omega = 4\pi,\ \widetilde{\rho} = \widetilde{\mu} = \widetilde{\beta} = 1,\ \widetilde{M} = (0,0,0.5)$$

we have obtained the convergence displayed in figure 18. The computations are completed on a 2-D rectangular computational domain (which gives a 3-D cylinder) with cylindrical PML. In

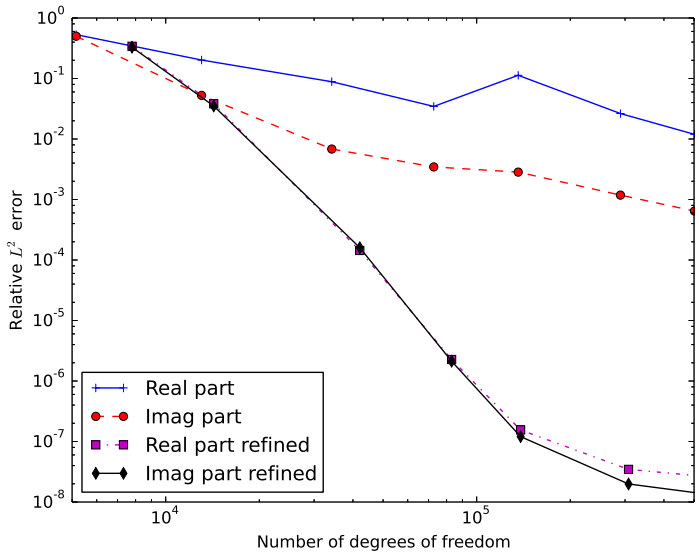


Figure 18: Relative $L^2$ error versus the number of degrees of freedom between the numerical Green's function and analytical one. Case of an uniform flow $\widetilde{M}_z = 0.5, \widetilde{\beta} = 1$, cylindrical PML are used.

this figure, we compare the case where an uniform refinement is performed and where a local refinement is also performed on the point $y$. Contrary to the uniform case without flow, the imaginary part also needs a local refinement to converge quickly to the correct solution.

# 4 Comparison between 1.5D, 2.5D method and 3D method

## 4.1 3-D method

The 3-D method is the classical finite element method. The computational domain is meshed in hexahedral elements:

$$\Omega \;=\; \bigcup_{i=1}^{N_e} K_i$$

The physical coefficients $\widetilde{\rho}$, $\widetilde{\mu}$, $\widetilde{M}$ and $\widetilde{\beta}$ and the geometry may depend on the three space variables $x$, $y$ and $z$. The solution $u$ is searched in the following finite element space

$$V_h \;=\; \left\{u \in H^1(\Omega) \text{ such that } u|_{K_i} \circ F_i \in \mathbb{Q}_r\right\}$$

where

$$\mathbb{Q}_r \;=\; \text{Span}\left\{\hat{x}^i \hat{y}^j \hat{z}^k, \quad 1 \leq i,j,k \leq r+1\right\}$$

The basis functions on the reference element $\hat{K}$ are products of 1-D basis functions for the unit cube :

$$\hat{\varphi}_i(\hat{x},\hat{y},\hat{z}) = \hat{\varphi}^{GL}_{i_1}(\hat{x})\hat{\varphi}^{GL}_{i_2}(\hat{y})\hat{\varphi}^{GL}_{i_3}(\hat{z})$$

where the 1-D basis functions $\hat{\varphi}^{GL}_i$ are based on Gauss-Lobatto points as explained in the previous section. The integrals are evaluated with the same Gauss-Lobatto points leading to faster computations. The basis functions on the real element are given by the relation

$$\hat{\varphi}_j = \varphi_j \circ F_i$$

The linear system issued from the variational formulation (2) can be solved either directly, either iteratively. The direct solver is MUMPS [1]. The iterative solver is the BICGCR (see [5]) preconditioned with a multigrid iteration (W-cycle). The multigrid iteration is based on the damped Helmholtz equation (see [9], [8]) with $\alpha = 1, \beta = 0.5$, the coarsest grid is $\mathbb{Q}_2$.

## 4.2 Efficiency of the different methods

The three numerical methods (3D, 2.5D and 1.5D) are compared for the case with uniform spherical layers previously described. $\mathbb{Q}_{10}$ elements are used, the mesh is designed such that for all the methods, the numerical error is similar (below $10^{-4}$). The 3-D mesh obtained for the 3D method is displayed in figure 19.

The solution is post-processed on a regular grid containing 120 000 points (three planes with 200x200 points each). In the table 1, the computational times are detailed, task by task. The task “Rhs” consists of computing the right hand sides for all the modes. The task “Factorization” consists of computing and factorizing the finite element matrices (or constructing the preconditioning). The task “LU sweeps” consists of solving the linear systems by using the LU factorization of finite element matrix involved while the task “Solve” is the time spent by the iterative solver in 3-D to converge to the solution (with a stopping criterion equal to $10^{-6}$). The task “Grid” consists of searching for each point of the output regular grid the element where the point is, and its local coordinates. The task “Interpolation” consists of computing the solution on points of the output regular grid.

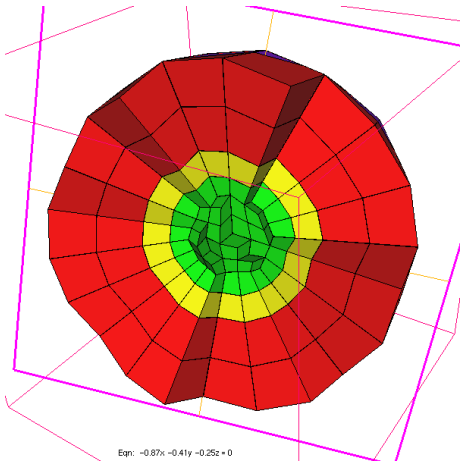

Figure 19: 3-D mesh used for the scattering of spherical layers

We see that in 1.5D and 2.5D the computational time is dominated by post-processing tasks whereas in 3-D the computational time is dominated by the solution of the linear system. The iterative solver is here much more efficient since the number of preconditioned iterations is small (equal to 60 for this case). The computational time and used memory are summarized in the table 2. In this table, the computational time does not include the post-processing tasks (Interpolation and Grid), the memory is measured with the command top. We observe that the 3-D method requires a large amount of memory if a direct solver is used. The memory usage of the 2.5D method is reasonable. Based on this comparison, we have preferred 1.5D and 2.5D methods for the rest of the document.

Table 1: Computation times for the different methods. From left to right, 1.5D method, 2.5D, 3D (with a direct solver) and 3D (with an iterative solver)

| Task | Time | Task | Time | Task | Time | Task | Time |
|---|---|---|---|---|---|---|---|
| Rhs | 42ms | Rhs | 0.42s | Rhs | 0.2s | Rhs | 0.2s |
| LU sweeps | 7.5ms | LU sweeps | 0.22s | LU sweeps | 2.7s | Solve | 35s |
| Factorization | 4.1ms | Factorization | 4.47s | Factorization | 522 s | Factorization | 23s |
| Grid | 26ms | Grid | 2.12s | Grid | 28.3s | Grid | 28.3s |
| Interpolation | 5.7s | Interpolation | 25.2s | Interpolation | 2s | Interpolation | 2.1s |
| Total 1.5D | 5.79s | Total 2.5D | 32.5s | Total Direct | 586s | Total Iterative | 95s |

Table 2: Efficiency of the different methods for spherical layers.

| Method | 1.5D | 2.5D | 3D (direct) | 3D (iterative) |
|---|---|---|---|---|
| # dofs | 56 129 | 307 575 | 453 001 | 453 001 |
| Time | 55.1 ms | 5.18 s | 556 s | 64.6 s |
| Memory | 128 Mo | 173 Mo | 26.3 Go | 535 Mo |

# 5 Application to helioseismology

The fluid displacement $\xi$ of the sun satisfies Galbrun's equations (cf. [11]):

$$\left(\frac{\partial}{\partial t} + \gamma + M\cdot\nabla\right)^2 \xi - \frac{1}{\rho}\nabla\left(\rho c^2 \mathrm{div}\xi\right) = F$$

where pressure and gravity terms are dropped. $\rho$ and $c$ are the background density and sound of speed, $M$ is the stationary flow, $F$ a given source. The flow is supposed to have a vanishing normal component on the boundary $\Gamma$:

$$M\cdot n = 0 \text{ on } \Gamma$$

and satisfy the mass conservation:

$$\mathrm{div}\,(\rho M) = 0$$

$\gamma$ is an ad-hoc damping which is added to the original equations. Fourier transform is applied to this equation with the convention $e^{-i\omega t}$ in order to obtain a time-harmonic equation:

$$-\left(\omega + i\gamma + iM\cdot\nabla\right)^2 \xi - \frac{1}{\rho}\nabla\left(\rho c^2 \mathrm{div}\xi\right) = F \tag{6}$$

**Proposition 5.1** *The unknown $u = \rho c^2\, div\,\xi$ satisfies the following equation*

$$\begin{aligned} -(\omega^2 + 2i\gamma\omega)\frac{u}{\rho c^2} + \frac{M}{c}\cdot\nabla\left(\frac{1}{\rho c}M\cdot\nabla u\right) - \frac{M\cdot\nabla(\rho c)}{\rho^2 c^3}M\cdot\nabla u - \frac{2i\omega}{c}M\cdot\nabla\left(\frac{u}{\rho c}\right) \\ -div\left(\frac{1}{\rho}\nabla u\right) = div\,F \end{aligned} \tag{7}$$

*by assuming a slowly variable background (i.e. terms in $\nabla\rho$ or $\nabla c$ are dropped), and a small damping $\gamma$.*

**Proof 1** *We take the divergence of the equation (6) and we multiply by $c$ to obtain:*

$$-(\omega+i\gamma)^2 c\, div\,\xi + c\, div\left((M\cdot\nabla)^2\xi\right) - 2ic(\omega+i\gamma)\, div\,(M\cdot\nabla\xi) - c\, div\left(\frac{1}{\rho}\nabla\left(\rho c^2\, div\,\xi\right)\right) = c\, div\, F$$

*When the damping $\gamma$ is small, we use the approximation:*

$$-(\omega+i\gamma)^2 \approx -(\omega^2 + 2i\gamma\omega)$$

*When $\rho$, $c$ and $M$ are slowly varying, $\rho$, $c$ and $div$ can be swapped with $M\cdot\nabla$ to obtain the following approximation:*

$$c\, div\left((M\cdot\nabla)^2\xi\right) \approx M\cdot\nabla\left(\frac{1}{\rho c}M\cdot\nabla\left(\rho c^2\, div\,\xi\right)\right) - \frac{M\cdot\nabla(\rho c)}{(\rho c)^2}M\cdot\nabla\left(\rho c^2\, div\,\xi\right)$$

*The second term is here artificially added in the final aim to obtain a variational formulation without gradients of $\rho$ or $c$. For a small damping $\gamma$ and slowly varying $c$ and $M$, we have:*

$$2ic\,(\omega+i\gamma)\, div\,(M\cdot\nabla\xi) \approx 2i\omega M\cdot\nabla\,(c\, div\,\xi)$$

*With these approximations and by using $u = \rho c^2 div\xi$, the following equation is obtained:*

$$-(\omega^2+2i\gamma\omega)\frac{u}{\rho c}+M\cdot\nabla\left(\frac{1}{\rho c}M\cdot\nabla u\right)-\frac{M\cdot\nabla(\rho c)}{(\rho c)^2}M\cdot\nabla u-2i\omega M\cdot\nabla\left(\frac{u}{\rho c}\right)-c\,div\left(\frac{1}{\rho}\nabla u\right)=c\,div\,F$$

*The final equation is then obtained by diving by $c$.*

The obtained equation is different from the model equation (1), but the variational formulation is similar to (2) as proven by the following proposition:

**Proposition 5.2** *The variational formulation of (7) is given as:*

$$-\left(\omega^2+2i\gamma\omega\right)\int_\Omega\frac{1}{\rho c^2}u\,\bar v\,dx+\int_\Omega\frac{1}{\rho c^2}M\cdot\nabla u\,M\cdot\nabla\bar v\,dx-i\omega\int_\Omega\frac{1}{\rho c^2}M\cdot\nabla u\,\bar v\,dx$$
$$+i\omega\int_\Omega\frac{1}{\rho c^2}M\cdot\nabla\bar v\,u\,dx+\int_\Omega\frac{1}{\rho}\nabla u\cdot\nabla\bar v\,dx-\int_\Omega\frac{1}{\rho}\frac{\partial u}{\partial n}\bar v\,dx=\int_\Omega div\,F\,\bar v\,dx$$

**Proof 2** *Let us multiply the equation (7) by the conjugate of a test function $v$ and integrate over the domain $\Omega$. The first term is not modified:*

$$-\left(\omega^2+2i\gamma\omega\right)\int_\Omega\frac{1}{\rho c^2}u\,\bar v\,dx$$

*An integration by parts is performed on the second term:*

$$\int_\Omega\frac{M}{c}\cdot\nabla\left(\frac{1}{\rho c}M\cdot\nabla u\right)\bar v\,dx=-\int_\Omega div\left(\frac{M}{c}\right)\bar v\,\frac{1}{\rho c}M\cdot\nabla u\,dx-\int_\Omega\frac{1}{\rho c^2}M\cdot\nabla u\,M\cdot\nabla\bar v\,dx$$

*The boundary term is here null because $M\cdot n=0$ on the boundary. Then, we compute the divergence of $M/c$ by using $div(\rho M)=0$ :*

$$div\left(\frac{M}{c}\right)=div\left(\frac{\rho M}{\rho c}\right)=-\frac{\nabla(\rho c)}{\rho\,c^2}\cdot M$$

*As a result, the second term is equal to:*

$$\int_\Omega\frac{M}{c}\cdot\nabla\left(\frac{1}{\rho c}M\cdot\nabla u\right)\bar v\,dx=+\int_\Omega\frac{M\cdot\nabla(\rho c)}{\rho^2c^3}M\cdot\nabla u\,\bar v\,dx-\int_\Omega\frac{1}{\rho c^2}M\cdot\nabla u\,M\cdot\nabla\bar v\,dx$$

*We see here that the first term of this last expression is canceling with the third term of the variational formulation (which has been chosen to fulfill this objective). An integration by parts is performed on the half of the fourth term:*

$$-2i\omega\int_\Omega\frac{M}{c}\cdot\nabla\left(\frac{u}{\rho c}\right)\bar v\,dx=\;-i\omega\int_\Omega\frac{1}{\rho c^2}M\cdot\nabla u\,\bar v\,dx-i\omega\int_\Omega\frac{M}{c}\cdot\nabla\left(\frac{1}{\rho c}\right)u\,\bar v\,dx$$
$$+i\omega\int_\Omega div\left(\frac{M}{c}\right)\frac{1}{\rho c}\,u\,\bar v\,dx+i\omega\int_\Omega\frac{1}{\rho c^2}M\cdot\nabla\bar v\,u\,dx$$

*By using the computed expression of the divergence of $M/c$, it can be observed that the two middle terms are canceling out. The fourth term is then equal to:*

$$-2i\omega\int_\Omega\frac{M}{c}\cdot\nabla\left(\frac{u}{\rho c}\right)\bar v\,dx=-i\omega\int_\Omega\frac{1}{\rho c^2}M\cdot\nabla u\,\bar v\,dx+i\omega\int_\Omega\frac{1}{\rho c^2}M\cdot\nabla\bar v\,u\,dx$$

*An integration by parts is performed on the fifth term:*

$$-\int_\Omega div\left(\frac{1}{\rho}\nabla u\right)\,\bar{v}\,dx = \int_\Omega \frac{1}{\rho}\nabla u\cdot\nabla\bar{v}\,dx - \int_\Gamma \frac{1}{\rho}\frac{\partial u}{\partial n}\,\bar{v}\,ds$$

*By summing all these terms, we obtain the claimed variational formulation.*

This variational formulation is the same as (2) with the following choices:

$$\widetilde{\rho} = \frac{1}{\rho c^2}\left(1+\frac{2i\gamma}{\omega}\right),\ \widetilde{M} = \frac{M}{\rho c^2},\ \widetilde{\mu} = \frac{1}{\rho},\ \widetilde{\beta} = \rho c^2,\ f = \mathrm{div}F$$

## 5.1 Numerical validation

As a first test, we have chosen analytical expressions for $\rho, c, \gamma$ and $M$ in order to check that the equation (7) is satisfied with the numerical method. In this subsection, the computations are performed in 2.5D for a single mode $m = 2$. We have considered the following parameters (we use cylindrical coordinates):

$$\rho = \exp\left(-\frac{r_{\mathrm{sph}}^2}{16}\right),\ c = e^{-0.6r_{\mathrm{sph}}}\left(1+0.8r_{\mathrm{sph}}+0.1r_{\mathrm{sph}}^2\right),\ \omega = 2\pi,\ \gamma = \frac{1}{200}$$

$$\rho M_r = \frac{xz}{x^2+z^2}(u_s(r_{\mathrm{sph}})-v_s(r_{\mathrm{sph}})),\ \rho M_\theta = \frac{x^2+z^2}{20},\ \rho M_z = \frac{1}{x^2+z^2}\left(z^2u_s(r_{\mathrm{sph}})+x^2v_s(r_{\mathrm{sph}})\right)$$

where

$$r_{\mathrm{sph}}^2 = r^2+z^2,\ u_s(r_{\mathrm{sph}}) = J_{10}\left(\frac{r_{\mathrm{sph}}}{r_t}\right),\ v_s(r_{\mathrm{sph}}) = u_s(r_{\mathrm{sph}})+\frac{r_{\mathrm{sph}}}{2}\,u_s'(r_{\mathrm{sph}})$$

The flow $M$ as been chosen such that the divergence of $\rho M$ is null and $M\cdot n = 0$ on the extern boundary $r = 4$. To satisfy this last condition, we choose

$$r_t \approx 0.27632895653242373$$

such that the Bessel function $J_{10}$ vanishes on the extern circle. The solution obtained for this mode (m=2) is displayed in the figure 20 (an example of mesh is also represented). In the figure 21, the consistency error is plotted against the mesh size $h/r$ where $r$ is the order of approximation. The consistency error is defined as the following quantity

$$\text{Consistency error} = \frac{||\mathrm{Eq1}(u^m)-\mathrm{Eq2}(u^m)||}{||\mathrm{Eq2}(u^m)||}$$

where $u^m$ is the solution for the selected mode and

$$\mathrm{Eq1}(u) = -(\omega^2+2i\gamma\omega)\frac{u}{\rho c^2}+\frac{M}{c}\cdot\nabla\left(\frac{1}{\rho c}M\cdot\nabla u\right)-\frac{M\cdot\nabla(\rho c)}{\rho^2c^3}M\cdot\nabla u-\frac{2i\omega}{c}M\cdot\nabla\left(\frac{u}{\rho c}\right)$$

$$\mathrm{Eq2}(u) = \mathrm{div}\left(\frac{1}{\rho}\nabla u\right)$$

We recognize the two terms of the equation (7). The norm used to evaluate this consistency error is not the usual $L^2$ norm, but a median norm, i.e. we sort all the values, and we pick

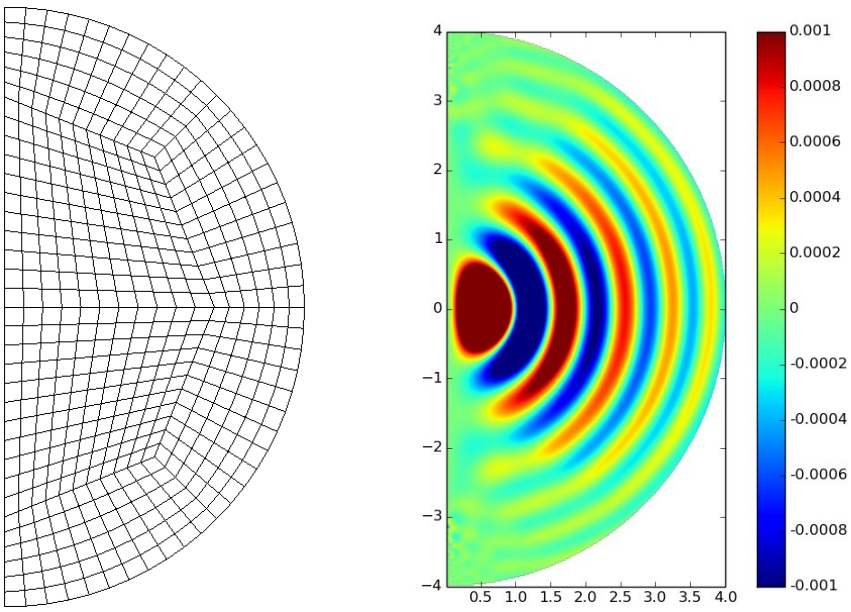


Figure 20: Solution for a single mode $m = 2$ with analytical values for $\rho, c, \gamma$ and $M$. On the left: example of used mesh, on the right: imaginary part of the solution.

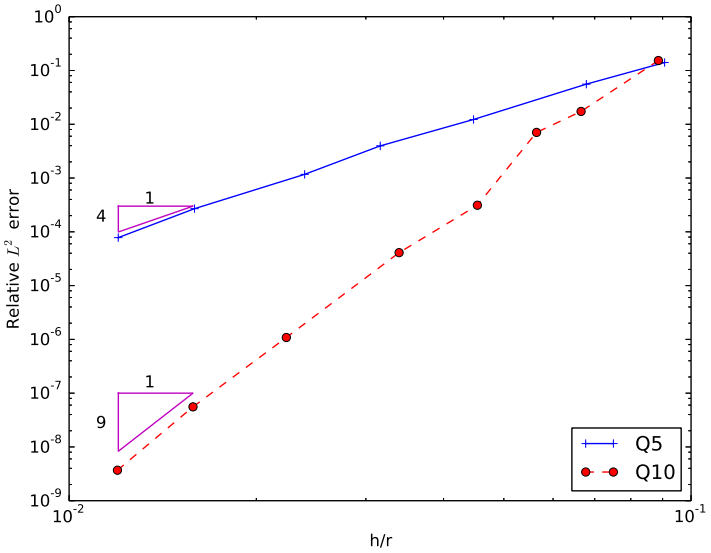


Figure 21: Consistency error versus $h/r$ for $\mathbb{Q}_5$ and $\mathbb{Q}_{10}$ for analytical values of $\rho, c, \gamma$ and $M$.

the value located at 90 % (instead of 50 %). This procedure is used to avoid problems on the axis Oz and in the vicinity of the source. The source is a Gaussian of center $(0.5, 0, 0)$ and of radius 0.6, the solution is measured on the $(x, z)$ plane $[0.01, 4] \times \{0\} \times [-4, 4]$ with $400 \times 400$

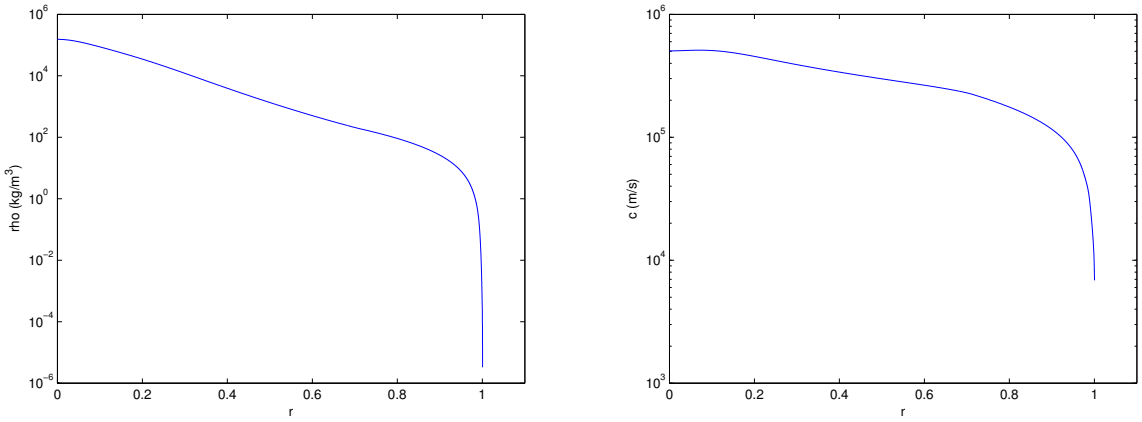


Figure 22: On the left: density $\rho$ versus the radius $r$, on the right: sound speed $c$.

points. This consistency error measures how well the equation is correctly satisfied. Since we have second-order derivatives, the numerical method converges in $O(h^{r-1})$ for this error.

## 5.2 Numerical results for 1.5D method

In this section, we are using the 1.5D method. Let us denote

$$\phi = \frac{u}{\sqrt{\rho}c^2}$$

The sun is assumed to be a perfect ball. The coefficients $\rho$ and $c$ are directly provided for different radii $r_i$ with realistic values of the sun (cf. the model S of [10]). The values for any $r$ are then obtained by a cubic spline interpolation, such that the coefficients are $C^2$-continuous. We take the following parameters

$$\omega = 2\pi f, \quad \gamma = \frac{\omega}{200}$$

The frequency $f$ is chosen as 3 mHz. An adimensionalization is performed such that this frequency (and $\gamma$) are multiplied by the radius of the sun (equal to $7 \cdot 10^8$ m) and a ball of radius 1.00069908 is considered. The flow is null in the following tests. An absorbing boundary condition is set on the outer sphere. This condition is not very well suited for the sun. Indeed, the sun does not have a defined boundary, but has an atmosphere which can be modeled by an exponentially decreasing density and a constant velocity (cf. [12]). More accurate boundary conditions are derived in [2] to mimic the presence of the atmosphere. In a first test, the 1-D mesh is chosen to coincide with the radii $r_i$ (therefore the mesh is adapted because the coefficients are polynomial on each element of the mesh). In the table 3, the relative $L^2$ error obtained for the unknown $\phi$ is computed versus the order of approximation for a Gaussian source (the distribution radius of the source is equal to 0.1).

The solution is represented in figures 23 and 24 for two different positions of the center of the Gaussian. The reference solution has been computed with multiple precision accuracy

Table 3: Relative $L^2$ error versus the order of approximation. Case of a Gaussian source located at the center of the domain.

| Order | Error | # dofs |
|---|---|---|
| 1 | $1.60 \cdot 10^{-3}$ | 2484 |
| 2 | $3.24 \cdot 10^{-6}$ | 4967 |
| 3 | $1.84 \cdot 10^{-8}$ | 7450 |
| 4 | $2.44 \cdot 10^{-10}$ | 9933 |
| 5 | $1.71 \cdot 10^{-11}$ | 12416 |

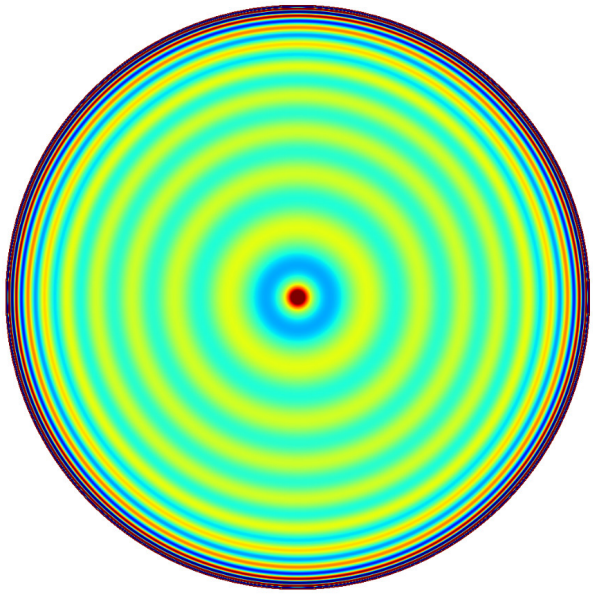

Figure 23: Real part of $\phi$ for a Gaussian source of center $(0, 0)$ and radius 0.1.

($\varepsilon \approx 10^{-60}$) with $\mathbb{Q}_{10}$ finite elements. The relative $L^2$ error is computed on the plane Oxz with $200 \times 200$ points. As it can be observed, the solution converges exponentially since the mesh is adapted to the medium and the source is smooth.

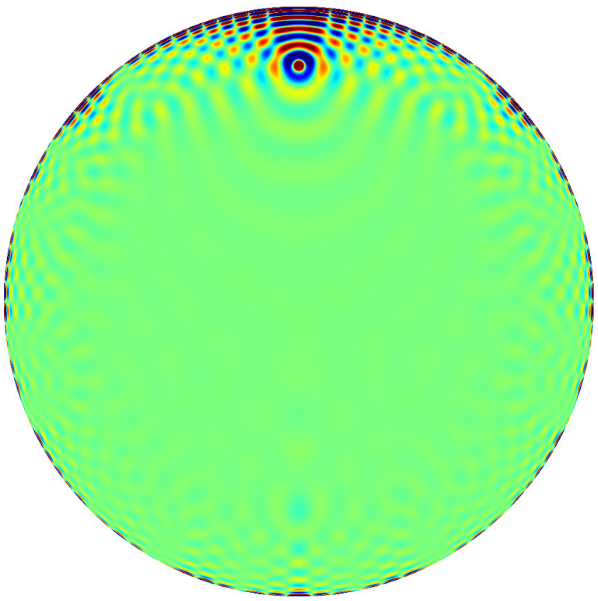

Figure 24: Real part of $\phi$ for a Gaussian source of center $(0, 0.8)$ and radius 0.02.

Table 4: Relative $L^2$ error versus the order of approximation for non-adapted meshes. Case of a Gaussian source located at $r = 0.8$.

| Error ($\mathbb{Q}_2$) | # dofs |
|---|---|
| $7.571 \cdot 10^{-2}$ | 147 |
| $3.102 \cdot 10^{-2}$ | 217 |
| $1.443 \cdot 10^{-3}$ | 429 |
| $6.068 \cdot 10^{-4}$ | 861 |
| $1.070 \cdot 10^{-4}$ | 1431 |

| Error ($\mathbb{Q}_4$) | # dofs |
|---|---|
| $9.747 \cdot 10^{-3}$ | 137 |
| $7.115 \cdot 10^{-3}$ | 217 |
| $2.361 \cdot 10^{-4}$ | 421 |
| $5.611 \cdot 10^{-5}$ | 857 |
| $7.952 \cdot 10^{-5}$ | 1433 |

| Error ($\mathbb{Q}_8$) | # dofs |
|---|---|
| $7.664 \cdot 10^{-3}$ | 145 |
| $3.829 \cdot 10^{-3}$ | 217 |
| $3.025 \cdot 10^{-4}$ | 425 |
| $1.644 \cdot 10^{-5}$ | 857 |
| $8.593 \cdot 10^{-7}$ | 1433 |

1-D meshes are generated by trying to satisfy a rule of N points per wavelength. The wavelength $\lambda(r)$ is computed with the following formula :

$$\lambda(r) = \min\left(\frac{2\pi}{k^-}, \frac{2\pi}{k^+}\right), \quad k^+ = i\frac{\alpha(r)}{2} + \sqrt{k^2(r) - \left(\frac{\alpha(r)}{2}\right)^2}, \quad k^- = i\frac{\alpha(r)}{2} - \sqrt{k^2(r) - \left(\frac{\alpha(r)}{2}\right)^2}$$

where

$$k(r) = \frac{\omega}{c(r)}, \ \alpha(r) = -\frac{\rho'(r)}{\rho(r)}$$

The 1-D meshes are constructed by starting from the right extremity and decrementing the position with the computed wavelength at each new position. With this family of meshes, we study the convergence of the numerical method in the table 4, for $\mathbb{Q}_2$, $\mathbb{Q}_4$ and $\mathbb{Q}_8$ for a Gaussian source centered at $(0, 0, 0.8)$ and of radius 0.02, 600 modes are used in $\ell$ ($L = 600$). We see that using second-order ($\mathbb{Q}_2$) elements is clearly less accurate and requires more degrees of freedom than for other orders of approximation. The results provided with $\mathbb{Q}_8$ are slightly more accurate.

Since the meshes are not adapted and the medium is not very smooth, there is no clear advantage in using very high order approximations. Moreover the $L^2$ error does not always decrease when the mesh is refined. A solution to this problem consists in constructing smooth approximations

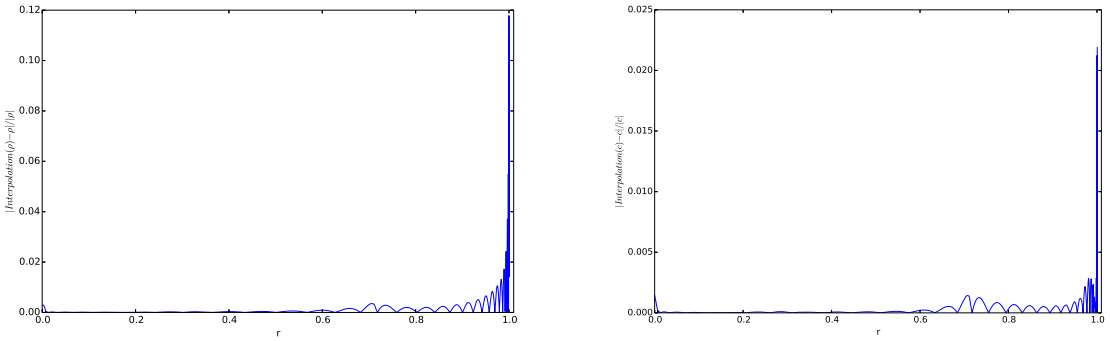


Figure 25: Relative error (pointwise) between the smooth approximations of $\rho$ and $c$ and raw values.

of $\rho$ and $c$. This task is achieved by using eighth-order B-splines, the knots of the spline are chosen from a 1-D mesh containing 26 vertices. The relative pointwise error made on $\rho$ and $c$ is displayed in the figure 25. As it can be seen, the error is large close to the surface of the sun. The solution computed with these approximations of $\rho$ and $c$ is qualitatively close to the solution computed with raw values (a relative $L^2$ error of 30 % has been measured). The different orders of approximation are compared in the table 5 with these smooth approximations. The meshes are not adapted to the medium, but since the medium is smooth enough ($C^8$), we obtain a fast convergence. We see that using $\mathbb{Q}_8$ is clearly more accurate.

Table 5: Relative $L^2$ error versus the order of approximation for smooth approximations of $\rho$ and $c$. Case of a Gaussian source located at $r = 0.8$.

| Error ($\mathbb{Q}_2$) | # dofs |
|---|---|
| $7.486 \cdot 10^{-2}$ | 147 |
| $2.535 \cdot 10^{-2}$ | 217 |
| $6.467 \cdot 10^{-4}$ | 429 |
| $4.259 \cdot 10^{-5}$ | 861 |
| $5.557 \cdot 10^{-6}$ | 1431 |

| Error ($\mathbb{Q}_4$) | # dofs |
|---|---|
| $1.183 \cdot 10^{-3}$ | 141 |
| $1.306 \cdot 10^{-4}$ | 217 |
| $2.456 \cdot 10^{-5}$ | 429 |
| $1.028 \cdot 10^{-6}$ | 865 |
| $9.643 \cdot 10^{-8}$ | 1413 |

| Error ($\mathbb{Q}_8$) | # dofs |
|---|---|
| $2.409 \cdot 10^{-4}$ | 145 |
| $1.640 \cdot 10^{-6}$ | 233 |
| $3.493 \cdot 10^{-8}$ | 433 |
| $9.039 \cdot 10^{-9}$ | 857 |
| $2.147 \cdot 10^{-10}$ | 1417 |

In the figure 26, we have displayed the relative $L^2$ error for a Gaussian source and a Dirac source versus $L$ (the number of modes in $\ell$). The source is located at $(0, 0, 0.8)$ with a radius of 0.02 for the Gaussian. The reference solution is computed with the 2.5D method (with an adapted mesh) with smoothed approximations of the sun such that the $L^2$ error is below $10^{-10}$ for this reference solution. The solutions are compared on $200 \times 200$ points on the plane Oxz. For this source, the imaginary part is easier to approximate accurately. When the source is located

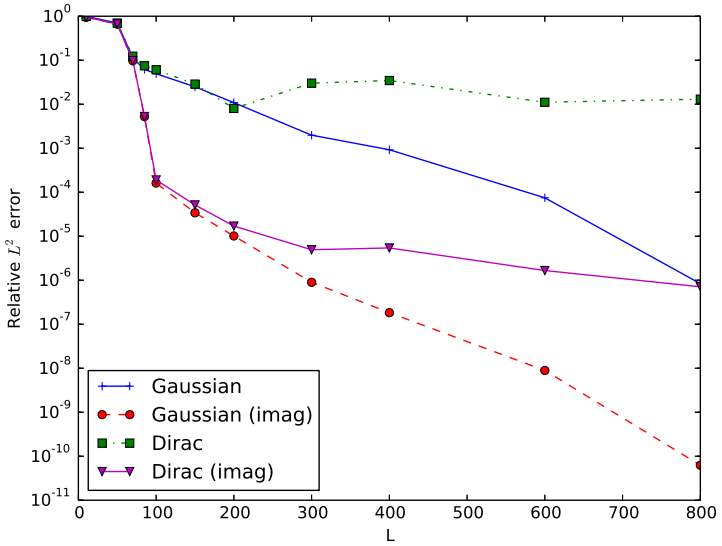


Figure 26: Relative $L^2$ error versus $L$ for two sources (in both cases, the center is located at (0,0,0.8)). The complex solution is compared or only the imaginary part.

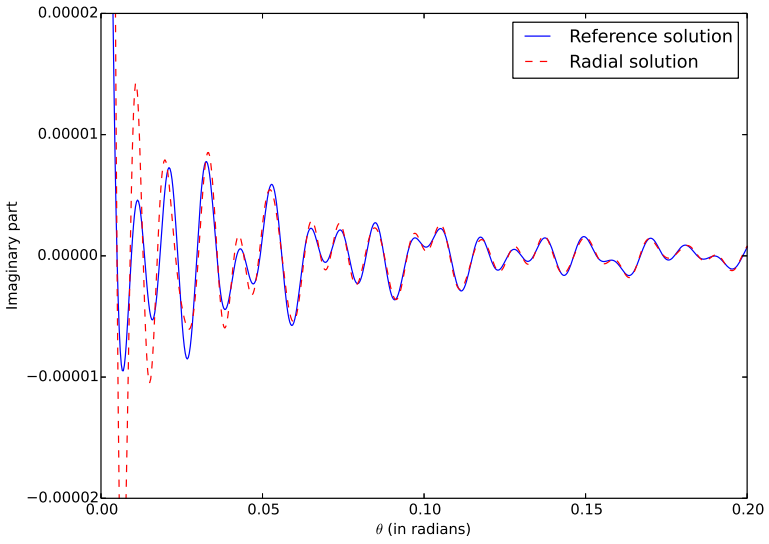


Figure 27: Imaginary part of the numerical Green's function versus $\theta$ for a point $y = (0, 0, 1.0001943)$. This solution is computed with 2.5D method (reference) and with 1.5D method with $L = 800$ modes in $\ell$.

at $(0, 0, 1.0001943)$, the number of needed modes in $\ell$ becomes very large to obtain an accurate

solution. In the figure 27, the imaginary part of the numerical Green's function is plotted versus $\theta$ on a circle of radius 1.0001943 for the reference solution (computed with the 2.5D method) and for the radial method with 800 modes in $\ell$. It can be observed that close to the source ($\theta = 0$) the solution obtained with the radial method is not accurate. As a result, the $L^2$ error computed on this circle provides an error of 80 %.

## 5.3 Numerical results for 2.5D method

The family of meshes used to run the 2.5D method are generated by starting from an uniform mesh of a disk $r \leq 0.7$, then circular layers are added to match the radii prescribed by the wavelength (this strategy has been described in the previous subsection), and a refinement in $\theta$ is performed to match the following wavelength (with $\alpha(r) = 0$):

$$\lambda_0(r) = \frac{2\pi}{k(r)}$$

If not specified, a local refinement will be performed close to the source in order to catch the singularity of the numerical Green's function. Moreover all the experiments presented in this subsection are performed when the point source is located on the axis Oz, such that only the mode $m = 0$ is computed. An example of mesh produced by this strategy is displayed in the

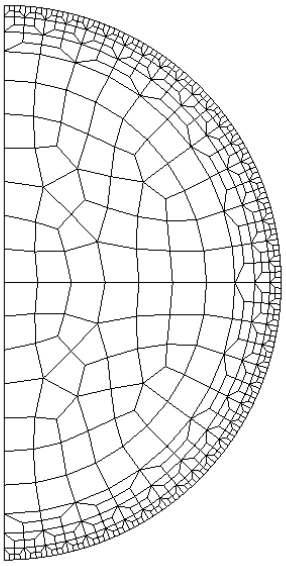

Figure 28: Example of mesh used for the 2.5D method.

figure 28. The convergence obtained for this family of meshes is represented in figure 29 for the computation of the Green's function ($y = (0, 0, 0.8)$). The solutions are compared on $200 \times 200$ points in the plane Oxz. It can be observed that $\mathbb{Q}_8$ approximation provides more accurate results than $\mathbb{Q}_4$ for a same number of degrees of freedom. In the figure 30, the $p$-convergence has been displayed, we can observe an exponential convergence as expected. For this figure, the

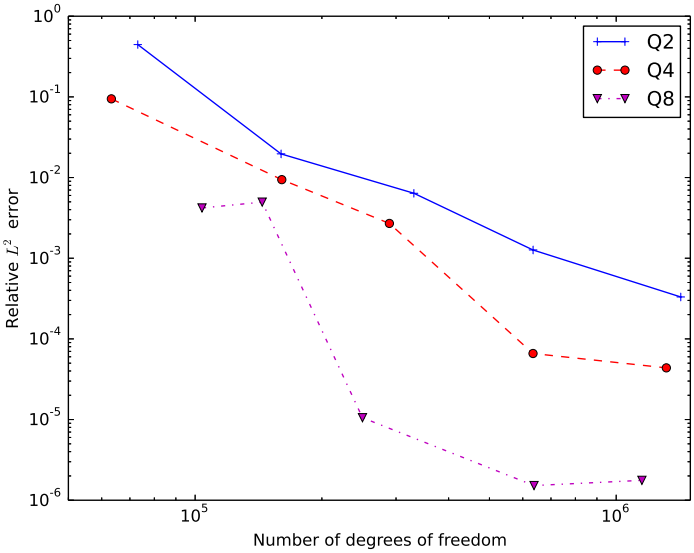


Figure 29: Relative $L^2$ error versus the number of degrees of freedom for $\mathbb{Q}_2$, $\mathbb{Q}_4$ and $\mathbb{Q}_8$. Case of a Dirac located at $(0, 0, 0.8)$.

solutions have been compared on a circle of radius 0.8 or 1.0001943 depending on the location of the Dirac source, only the imaginary parts have been compared. In the figure 31, we can observe that a local refinement is necessary if we want a good resolution for the imaginary part of the numerical Green's function close to the source. In the table 6, we have displayed the number of dofs needed to obtain a discrete $L^2$ error (computed with 20000 points on the circle of radius 1.0001943 for the imaginary part of the solution) between $10^{-3}$ and $2 \cdot 10^{-3}$. The number of degrees of freedom is not proportional to $\omega^2$ as it could be expected because of the complex wavelengths $\lambda^+$ and $\lambda^-$ whose expressions have been given in the previous subsection. It can

Table 6: Number of degrees of freedom needed for different frequencies to obtain an accurate approximation of the Green's function (the center of the Dirac is located on the point $(0, 0, 1.0001943)$).

| Frequency | 3mHz | 6mHz | 9mHz | 12mHz |
|---|---|---|---|---|
| # Dofs | 322 301 | 407 951 | 605 041 | 951 641 |
| Error | $1.43 \cdot 10^{-3}$ | $1.75 \cdot 10^{-3}$ | $1.93 \cdot 10^{-3}$ | $1.89 \cdot 10^{-3}$ |

be observed that the choice of the axisymmetric method (2.5D) enables us to handle cases of practical interest (for which the frequency is lower than 12 mHz).

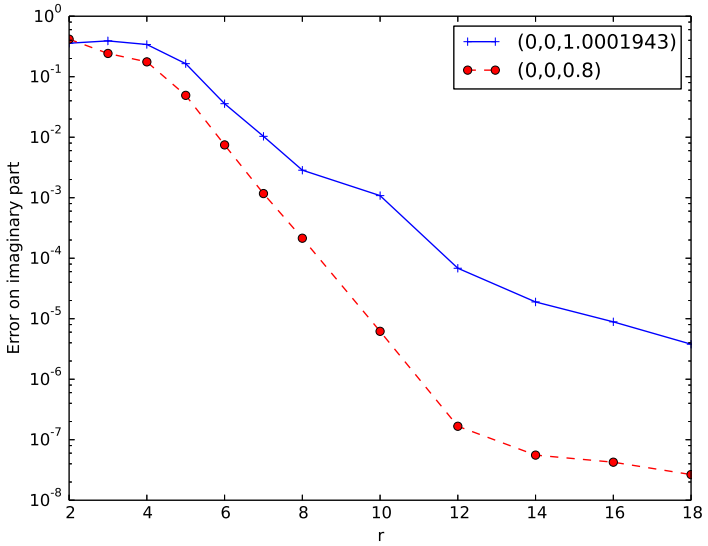


Figure 30: Relative $L^2$ error versus the order of approximation. Case of a Dirac located at $(0, 0, 0.8)$ or $(0, 0, 1.0001943)$. The error is based on imaginary part of the solution on points on a circle.

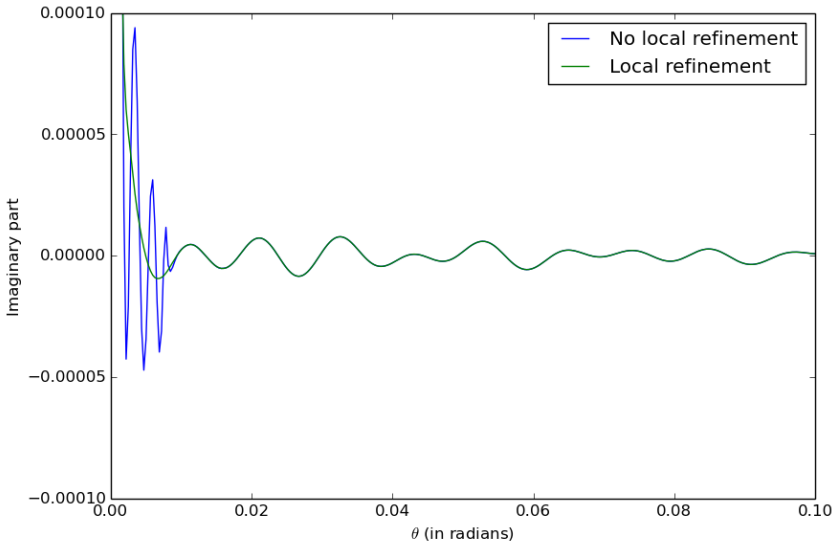


Figure 31: Imaginary part of the numerical Green's function for $y = (0, 0, 1.0001943)$. In blue, without local refinement and in green with a local refinement

# 6 Acknowledgements

Experiments presented in this paper were carried out using the PLAFRIM experimental testbed, being developed under the Inria PlaFRIM development action with support from LABRI and IMB and other entities: Conseil Régional d'Aquitaine, FeDER, Université de Bordeaux and CNRS (see https://plafrim.bordeaux.inria.fr/).

# A Analytical solutions for a sphere

Analytical solutions can be constructed for an incident plane wave without flow ($\widetilde{\beta} = \widetilde{M} = 0$). In this type of problem, u is searched as

$$u = u^{\text{inc}} + u^{\text{diff}}$$

where $u^{\text{diff}}$ is the diffracted field and $u^{\text{inc}}$ the incident plane wave. We choose a wave vector in the direction of the axis $Oz$ :

$$u^{\text{inc}} = \exp(ik_\infty z)$$

where $k_\infty$ is the wave number at the infinity. The diffracted field satisfies the Sommerfeld condition :

$$\lim_{r\to\infty} \frac{\partial u^{\text{diff}}}{\partial n} - ik_\infty u^{\text{diff}} = 0$$

In this section, we are using spherical coordinates (instead of cylindrical coordinates) :

$$\begin{cases} x = r\sin\theta\cos\varphi \\ y = r\sin\theta\sin\varphi \\ z = r\cos\theta \end{cases}$$

Then Jacobi-Anger's expansion provides :

$$\exp(ik_\infty z) \;=\; \exp(ik_\infty r\cos\theta) \;=\; \sum_{n=0}^{\infty} i^n(2n+1)j_n(k_\infty r)P_n(\cos\theta)$$

where $P_n$ are Legendre polynomials and $j_n$ are the spherical Bessel functions. These last functions are related to Bessel functions $J_\nu$ by the relation

$$j_n(x) \;=\; \sqrt{\frac{\pi}{2x}}J_{n+1/2}(x)$$

We consider $N$ spherical layers, with $\widetilde{\rho}$ and $\widetilde{\mu}$ constant on each layer :

$$(\widetilde{\rho}(x), \widetilde{\mu}(x)) = (\widetilde{\rho}_i, \widetilde{\mu}_i), \quad r_i \le x \le r_{i+1}$$

The radii $(r_i)_{0\le i\le N}$ are increasing :

$$r_0 < r_1 < r_2 \cdots r_{N-1} < r_N$$

If the first radius $r_0$ is equal to 0, the first layer is a dielectric ball. If the last radius $r_N$ is infinite, exact Sommerfeld condition is set, otherwise the Sommerfeld condition is set at the finite radius $r_N$ :

$$\left(\frac{\partial u^{\text{diff}}}{\partial r} - ik_{N-1}u^{\text{diff}}\right)(r_N) = 0$$

The wave numbers $k_i$ are defined as :

$$k_i = \omega\sqrt{\frac{\widetilde{\rho}_i}{\widetilde{\mu}_i}}$$

In the last layer $r \geq r_{N-1}$, the total field $u$ is searched as :

$$u \;=\; \sum_{n=0}^{\infty} i^n (2n+1) \left[ j_n(k_{N-1} r) + \alpha_n^{N-1} h_n^{(1)}(k_{N-1} r) + \beta_n^{N-1} h_n^{(2)}(k_{N-1} r) \right] P_n(\cos\theta)$$

where $h_n^{(1)}$ and $h_n^{(2)}$ are spherical Hankel functions of the first and second kind. We note also $y_n$ the spherical Bessel function of the second kind, we have the relationship

$$h_n^{(1)}(x) = j_n(x) + i y_n(x)$$

In an internal layer $r_i \leq r \leq r_{i+1}$, $u$ is searched as

$$u \;=\; \sum_{n=0}^{\infty} i^n (2n+1) \left[ \alpha_n^i h_n^{(1)}(k_i r) + \beta_n^i h_n^{(2)}(k_i r) \right] P_n(\cos\theta)$$

Because of this form, $u$ satisfy the appropriate Helmholtz equation on each layer. It suffices to express boundary conditions and transmission conditions in order to obtain the coefficients $\alpha_n^i, \beta_n^i$. These $2N$ coefficients are solving a linear system. The boundary condition imposed at $r = r_0$ will provide one equation. The transmission conditions will provide $2(N-1)$ equations (two equations by interface), and the boundary condition imposed at $r = r_N$ will provide the last equation, thus all the coefficients can be found. In the sequel, the different equations are detailed.

## Boundary condition at $r = r_0$

### Internal ball ($r_0 = 0$)

If $r_0 = 0$, only Bessel function $j_n$ are regular at the center, therefore we have the following equation

$$\alpha_n^0 = \beta_n^0$$

### Dirichlet condition ($r_0 \neq 0$)

If $u = 0$ for $r = r_0$, we have the following equation :

$$\alpha_n^0 h_n^{(1)}(k_0 r_0) + \beta_n^0 h_n^{(2)}(k_0 r_0) = -\delta_{N,1}\; j_n(k_0 r_0)$$

where $\delta$ is the Kronecker symbol. As we can see, this equation has a right hand side only when there is one layer.

### Robin condition ($r_0 \neq 0$)

If we have a Robin condition at $r = r_0$ :

$$\frac{\partial u}{\partial n} + \beta u = 0$$

We obtain the following equation

$$\alpha_n^0 \left( k_0 h_n^{'(1)}(k_0 r_0) + \beta h_n^{(1)}(k_0 r_0) \right) + \beta_n^0 \left( k_0 h_n^{'(2)}(k_0 r_0) + \beta h_n^{(2)}(k_0 r_0) \right) = -\delta_{N,1}\; \left( k_0 j_n'(k_0 r_0) + \beta j_n(k_0 r_0) \right)$$

### Transmission conditions at $r = r_i$

Across each interface, $u$ and $\widetilde{\mu}\dfrac{\partial u}{\partial n}$ are continuous. As a result, we obtain the two equations :

$$\begin{cases} \alpha_n^{i-1} h_n^{(1)}(k_{i-1}r_{i-1}) + \beta_n^{i-1} h_n^{(2)}(k_{i-1}r_{i-1}) - \alpha_n^{i} h_n^{(1)}(k_i r_{i-1}) - \beta_n^{i} h_n^{(2)}(k_i r_{i-1}) = \delta_{i,N-1} j_n(k_i r_{i-1}) \\ \alpha_n^{i-1} \widetilde{\mu}_{i-1} k_{i-1} h_n^{'(1)}(k_{i-1}r_{i-1}) + \beta_n^{i-1} \widetilde{\mu}_{i-1} k_{i-1} h_n^{'(2)}(k_{i-1}r_{i-1}) \\ \quad -\alpha_n^{i} \widetilde{\mu}_i k_i h_n^{'(1)}(k_i r_{i-1}) - \beta_n^{i} \widetilde{\mu}_i k_i h_n^{'(2)}(k_i r_{i-1}) = \delta_{i,N-1} \widetilde{\mu}_i k_i j_n'(k_i r_{i-1}) \end{cases}$$

### Boundary condition at $r = r_N$

#### Infinite medium

In this case, only $h_n^{(1)}$ satisfies the exact Sommerfeld condition, we therefore have the following equation:

$$\beta_n^{N-1} = 0$$

#### First-order absorbing boundary condition

If Sommerfeld condition is imposed at a finite distance $r_N$, we have the following equation :

$$\alpha_n^{N-1} \left( h_n^{'(1)}(k_{N-1}r_N) - i h_n^{(1)}(k_{N-1}r_N) \right) + \beta_n^{N-1} \left( h_n^{'(2)}(k_{N-1}r_N) - i h_n^{(2)}(k_{N-1}r_N) \right) = 0$$

## References


[1] P.R. Amestoy, I.S. Duff, J. Koster, and J.-Y. L'Excellent. A fully asynchronous multifrontal solver using distributed dynamic scheduling. *SIAM Journal on Matrix Analysis and Applications*, 23:15–41, 2001.

[2] Hélène Barucq, Juliette Chabassier, Marc Duruflé, and Laurent Gizon. Atmospheric radiation boundary conditions for the helmholtz equation. *to be submitted*, pages 1–14, 2016.

[3] Eliane Bécache, Anne-Sophie Bonnet-Ben Dhia, and Guillaume Legendre. Perfectly matched layers for the convected Helmholtz equation. Inria Research Report 4690, INRIA, 2003.

[4] D. Casalino and D. Bodony. Green's function discretization of Pridmore-Brown wave operator. In *Proceedings of the Summer Program 2006*, pages 547–558. Center for Turbulence Research, 2006.

[5] M. Clemens and T. Weiland. Iterative methods for the solution of very large complex symmetric linear systems of equations in electrodynamics. Fachbereich 18 elektrische nachrichtentechnik, Technische Hochschule Darmstadt, 2002.

[6] Francis Collino and Peter Monk. The perfectly matched layer in curvilinear coordinates. Inria Research Report 3049, INRIA, 1996.

[7] Francis Collino and Chrysoula Tsogka. Application of the perfectly matched absorbing layer model to the linear elastodynamic problem in anisotropic heterogeneous media. *Geophysics*, 66:294–307, 2001.

[8] M. Duruflé. *Intégration numérique et éléments finis d'ordre élevé appliqués aux équations de Maxwell en régime harmonique.* PhD thesis, Université Paris IX-Dauphine, 2006.

[9] Y. A. Erlangga, C. Vuik, and C.W. Osterlee. A novel multigrid based preconditioner for heterogeneous Helmholtz problems. Report of delft university technology, Delft University Technology, 2004.

[10] Christensen-Dalsgaard et al. The current state of solar modeling. *Science*, 272:1286–1292, 1996.

[11] D. Lynden-Bell and J.P. Ostriker. On the stability of differentially rotating bodies. *Mon. Not. R. astr. Soc.*, 136:293–310, 1967.

[12] H. Schunker, R.H. Cameron, L. Gizon, and H. Moradi. Constructing and characterising solar structure models for computational helioseismology. *Solar Physics*, 271, 2011.

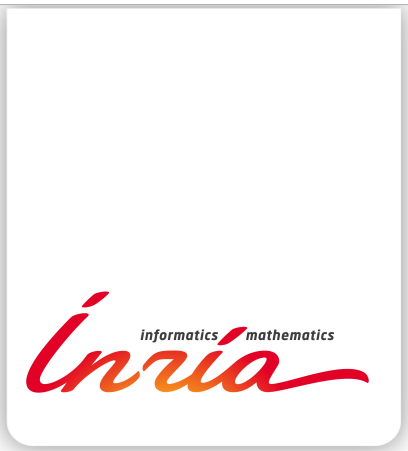


**RESEARCH CENTRE**
**BORDEAUX – SUD-OUEST**

200 avenue de la Vieille Tour
33405 Talence Cedex

Publisher
Inria
Domaine de Voluceau - Rocquencourt
BP 105 - 78153 Le Chesnay Cedex
inria.fr

ISSN 0249-6399